Hindawi
Structural Control and Health Monitoring
Volume 2023, Article ID 6618783, 26 pages
https://doi.org/10.1155/2023/6618783

Research Article

Active Vibration Control of Wind Turbine Using Virtual TMD Algorithm Based on Aerodynamic-Structure-Servo Coupling Model

Tao Long,[1,2,3] **Qingshan Yang**,[1] **Qi Wang**,[4] **Guoqing Huang**,[1] **Xuhong Zhou**,[1] **and Yu Yang**[1]

[1]*School of Civil Engineering, Chongqing University, Chongqing 400045, China*
[2]*Energy Research Institute, Qilu University of Technology (Shandong Academy of Sciences), Jinan, Shandong 250014, China*
[3]*Yangjiang Offshore Wind Energy Laboratory, Yangjiang, Guangdong 529500, China*
[4]*School of Civil Engineering and Architecture, Hainan University, Haikou 570228, China*

Correspondence should be addressed to Qi Wang; wangqi67315@126.com and Guoqing Huang; ghuang1001@gmail.com

Received 17 January 2023; Revised 10 September 2023; Accepted 22 September 2023; Published 10 October 2023

Academic Editor: Zili Zhang

In order to extract more wind energy, the wind turbine rotor becomes larger and the tower becomes taller. With more flexibility and smaller damping, wind turbine tower is prone to vibrate in winds. Meanwhile, the tower suffers the periodic loadings caused by the rotor rotation in the operational condition. The excessive vibrations could not only significantly affect the power generation but shorten the structural life due to the fatigue as well. It is challenging to reduce the vibration caused by the rotor rotation using the passive tuned mass damper (TMD) and traditional LQR controller due to the limited effective bandwidth. Therefore, an active tuned mass damper (ATMD) using a virtual TMD algorithm is proposed to mitigate the along-wind vibration of the tower under parked and operational conditions. The virtual TMD algorithm exhibits wide effective bandwidth and only requires the acceleration information on the top of the tower or the relative displacement of the active TMD. Firstly, the aerodynamic-structure-servo coupling (ASSC) model of the wind turbine is established which considers the interaction among the aerodynamic load, structure, and servo system. Secondly, the accuracy of the ASSC model is then verified using the onshore 5 MW wind turbine by the National Renewable Energy Laboratory (NREL). Thirdly, the ATMD feedback control force is designed by the virtual TMD algorithm. Finally, the reduction effect on the along-wind vibration by the proposed controller is evaluated at both of operational and parked conditions using the ASSC model. The TMD and LQR controller are utilized for comparison. The numerical results demonstrate that tuned mass damper (TMD) system with fixed parameters becomes detuned and may loses its effectiveness at different wind speeds. In contrast, active control can suppress the vibration of wind turbines at different wind speeds. Compared to the LQR controller, the proposed controller can enhance the reduction effect of wind turbine response with smaller stroke and control force at operational conditions.

1. Introduction

With the increasingly severe energy crisis and environmental pollution, renewable energies, especially wind energy, have attracted wide attention and become the key to the energy transition. The global installed wind power capacity has reached 906 GW by the end of 2022, and the increment is 77.6 GW within the year 2022 [1]. The increment of the global installed wind power capacity will be expected to reach 143 GW by the end of 2030, which is 13% higher than previous forecasts [1]. As the worldwide demand for wind power continues to increase, wind turbine hubs become taller and rotor diameters become larger to capture more wind energy and reduce the levelized cost of energy [2]. However, this trend leads to a reduction in wind turbine natural frequencies and structural damping ratios, resulting in a significant increase in wind-induced vibrations. Excessive wind-induced vibrations not only affect the normal

operation of wind turbines but also cause damage to wind turbines or even collapse. Dueñas-Osorio and Basu [3] indicated that the malfunctioning of acceleration-sensitive equipment in wind turbines might increase the annual failure rate during normal operating conditions. Colwell and Basu [4] showed that wind-induced vibrations may reduce the fatigue life of wind turbines. Chou and Tu [5] observed that wind turbines can cause structural damage and collapse under strong wind loads. From 2010 to 2022, there were 145 wind turbine accidents caused by structural failures worldwide, with a considerable proportion caused by wind-induced vibrations [6]. Thus, it is obvious that the vibration of wind turbines will not only adversely affect the production of electrical energy but also affect the structural safety. Therefore, it is necessary to reduce the vibration of wind turbines.

Different control strategies have been investigated to reduce the vibration of wind turbine towers and blades [7, 8]. Generally, there are three strategies for reducing the vibration of wind turbines: passive, semiactive, and active control. Passive control has been extensively studied on wind turbines over the past decades due to its simplicity of installation, convenient maintenance, low cost, and good stability. Studies have shown that a tuned mass damper system (TMD) can effectively suppress the vibration of wind turbine towers [9–14]. Zuo et al. [15] proposed multiple tuned mass dampers (MTMDs) to reduce the vibration of offshore wind turbine towers under parked conditions. The results showed that MTMDs can effectively control vibrations from the fundamental and higher modes of offshore wind turbine tower under the multihazards of the wind, wave, and earthquake. Many scholars have also proposed tuned mass-damper-inerter (TMDI) systems to suppress the vibration of wind turbines [16–18]. Their results have shown that the TMDI can reduce the structural response with a smaller mass ratio and stroke than traditional TMD. Chen and Georgakis [19] proposed a tuned rolling ball damper to control the bidirectional vibration of wind turbine. The experimental results demonstrated that this damper can effectively reduce the vibration of the wind turbine. Sun and Jahangiri [20] utilized a three-dimensional pendulum-tuned damper (3d-PTMD) to reduce the bidirectional vibration of wind turbine under the multihazards of the wind, wave, and earthquake. Their findings indicated that the 3d-PTMD can suppress the vibration of the wind turbine with a smaller stroke and a better control effect than dual linear passive TMDs. Mensah and Dueñas-Osorio [21] found that tuned liquid column dampers (TLCDs) can suppress the vibration of wind turbines, which can effectively reduce the vulnerability and improve the reliability of wind turbine towers. Although the passive control can effectively suppress the vibration of wind turbines under certain conditions, it may lose its effectiveness or even aggravate the structural vibration due to the complex environments and the time-varying characteristics of wind turbines. It is well known that wind turbine is a time-varying system. Ghassempour et al. [13] found that the optimal tuning frequency of TMD should vary with the wind speed to achieve the best vibration reduction effect. Consequently, the passive control based on conventional design may not be that appropriate for reducing wind-induced vibrations of wind turbines under various conditions.

Compared with passive control, the semiactive and active control can adjust their parameters in real time. Therefore, they are more suitable for wind turbine systems, especially under operational conditions. Hence, scholars have studied the semiactive and active control of wind turbines. For the semiactive control method, Chen et al. [22] developed a magnetorheological (MR) damper using a semiactive fuzzy control strategy, which can effectively suppress the in-plane vibration of wind turbine blades under extreme wind loads. Sun [23] and Hemmati and Oterkus [24] investigated the vibration reduction effect of the semiactive variable stiffness TMD on offshore monopile wind turbines subjected to the wind, wave, and earthquake. The authors found that the semiactive TMD adjusted in real time not only had more effectiveness in controlling the structural response but also had a smaller stroke than passive TMD. For the active control of wind turbines, ATMDs have been commonly used [8]. Different control algorithms have been proposed such as H infinity [25, 26], static state feedback [27–29], and adaptive sliding-mode [30]. In their studies, Lackner and Rotea [25] and Brodersen et al. [27] investigated the responses of offshore monopile wind turbine without dampers and with ATMD and TMD. Through frequency domain and time-domain analysis, it was shown that the vibration reduction effect of the ATMD was better than that of the TMD with the same mass ratio. Then, Li and Gao [26] proposed the generalized H infinity optimal approach to derive the control force for the ATMD. Their findings indicated that active control is more effective in reducing the primary fatigue load than passive control. Fitzgerald et al. [28, 29] explored the effectiveness of ATMD based on optimal LQR control in mitigating the responses of wind turbines. It was found that the active control strategy used achieved greater response reductions than the passive TMD. Hu et al. [30] proposed an adaptive sliding-mode controller to reduce the load of wind turbines. The finding indicated that the proposed control law improves the overall performance of the wind turbine under the consideration of the system uncertainties. The above findings show that semiactive and active control can adjust their own parameters in real time according to the time-varying characteristics of the structure, which can significantly reduce the vibration of wind turbines and have good robustness.

Although much research has been conducted to reduce the vibration of wind turbines using different control strategies, limitations in these strategies still exist. For operating wind turbines, the tower suffers the periodic (3P, 6P, etc.) loadings caused by the rotor rotation, which is different from the traditional high-rise structure [31]. The noticeable 3P frequency can be observed in the response of the wind turbine tower [32]. However, the principle of the vibration mitigation in the most aforementioned literature is to achieve vibration control by changing the transfer function of the structure. The response of the wind turbine at the natural frequency can be significantly reduced, while the control effect of the response at far away from the natural

frequency caused by the periodic loadings is not obvious. Perhaps the LQR controller for ATMD [28, 29] can effectively reduce the responses of the wind turbine, but there are still several limitations existing. Firstly, it is challenging to control two widely separated frequencies simultaneously using the LQR controller due to the limited effective bandwidth of the controller. Secondly, the LQR controller requires full states of wind turbines, and the obtainment of these states is a challenge for the measurement.

On the other hand, the wind turbine is a complicated dynamic system including the coupling effects among the aerodynamics, tower-nacelle-blade, and servo system. To accurately evaluate the system behavior, different models have been developed by scholars over the decades. Finite element models have been commonly adopted to study the wind-induced responses of the tower in structural analysis [33, 34]. Then, Jonkman and Marshall [35] developed a time-domain simulation tool called FAST in 2006, which utilizes Kane's equations to analyze the dynamic responses of wind turbines in depth. The accurate prediction of the wind turbine response is a prerequisite for vibration control research. Zhang [36] developed a reduced-order coupled model for wind turbines with 13 degrees of freedom using the Euler–Lagrangian together with nonlinear aerodynamics, which served as a basis for extensive research on passive and active vibration control. Zuo et al. [8] emphasized the importance of considering the influences of the coupling effects and the interactions among the components of wind turbines in vibration control research. Therefore, a fully coupled wind turbine model should be adopted in vibration control research to study the effectiveness of the proposed control method more accurately.

To address the 3P vibration problem of wind turbines with limited state measurement information, an active control method based on the virtual TMD is proposed and validated with an aerodynamic-structure-servo coupling model in this paper. The virtual TMD algorithm has a wide effective bandwidth and only requires the acceleration information on the top of the tower or the relative displacement of the active TMD. Firstly, an aero-structure-servo coupling model (ASSC model) will be established in MATLAB/Simulink for dynamic analysis of the wind turbine. Secondly, the accuracy of the ASSC model will be verified by comparative analysis with the wind turbine analysis package FAST (fatigue, aerodynamics, structures, and turbulence). Thirdly, an ATMD active controller is designed by the virtual TMD algorithm to suppress the vibration in the fore-aft (FA) direction of the wind turbine tower. Finally, compared with passive TMD and the traditional LQR algorithm, the established model is utilized to evaluate the vibration reduction effect of the virtual TMD algorithm on the wind turbine under different conditions.

2. The Holistic Coupled Model

In this section, a holistic coupled model of an aero-structure-servo system is established, including the aerodynamic module, structural module, and servo system module, which is named as the ASSC model in the paper. The aerodynamic module is mainly adopted to determine the aerodynamic loading of the structure by using wind field information and the responses of the wind turbine. The structural module is used to obtain the responses of the wind turbine according to aerodynamic loadings and commands of the servo system. The servo system module is generally utilized to control the rotating speed and pitch angle of the blade based on the wind speed and dynamic response characteristics.

2.1. Structure Model. The structural model of the wind turbine is established by using the Lagrangian equation. The equation is as follows:

$$\frac{\mathrm{d}}{\mathrm{d}t}\frac{\partial T\left(t,\mathbf{q}\left(t\right),\dot{\mathbf{q}}\left(t\right)\right)}{\partial \dot{q}_i\left(t\right)}-\frac{\partial T\left(t,\mathbf{q}\left(t\right),\dot{\mathbf{q}}\left(t\right)\right)}{\partial q_i\left(t\right)}+\frac{\partial V\left(t,\mathbf{q}\left(t\right)\right)}{\partial q_i\left(t\right)}=Q_i\left(t\right), \tag{1}$$

where T and V are the system kinetic and potential energy, $\mathbf{q}(t)$ is the generalized coordinates vector, $Q_i(t)$ is the generalized force corresponding to the ith component of $\mathbf{q}(t)$, and dot $(\cdot)$ represents the first derivative with respect to time.

To simplify the complex physical model of the wind turbine, the following assumptions are given as follows:

(1) A wind turbine consists of blades, hub, nacelle, and tower. The blade and tower are modeled as elastic cantilevers, the hub and nacelle are assumed to be the lumped mass, and a rigid connection is assumed among the rotor, nacelle, and tower [35, 37, 38].

(2) It is assumed that the bottom of the tower is fixed to the ground. The nacelle is fixed on the top of the tower, while there is a certain distance from the top of the tower to the center of mass of the nacelle [37]. The rotor is composed of three blades, which are connected with a nacelle through the hub. The nacelle yaw is neglected in the model [12].

(3) The response of the tower and blades is dominated by the contribution of the fundamental mode, neglecting the influence of the higher modes [20, 28].

2.1.1. Coordinate System of the Structure Model. The wind turbine is a rotating system composed of multiple components. In order to determine the distribution of load, displacement, velocity, and other vectors in time and space when establishing equations, it is necessary to build multiple coordinate systems, which is convenient for the conversion among wind turbine components. The simplified model is illustrated in Figure 1(a), which is described by four coordinate systems, as shown in Figure 1(b). First, the global coordinate system C_0 is established at the bottom of the tower. The tower-top coordinate system C_1 is nonrotating and located at the center of the tower top. The hub coordinate system C_2 is fixed on the rotating shaft. The blade section coordinate system C_3 is aligned with one of the blades. As the rotor rotates, the angle between the y_b-z_b and y_h-z_h planes is the azimuth angle.

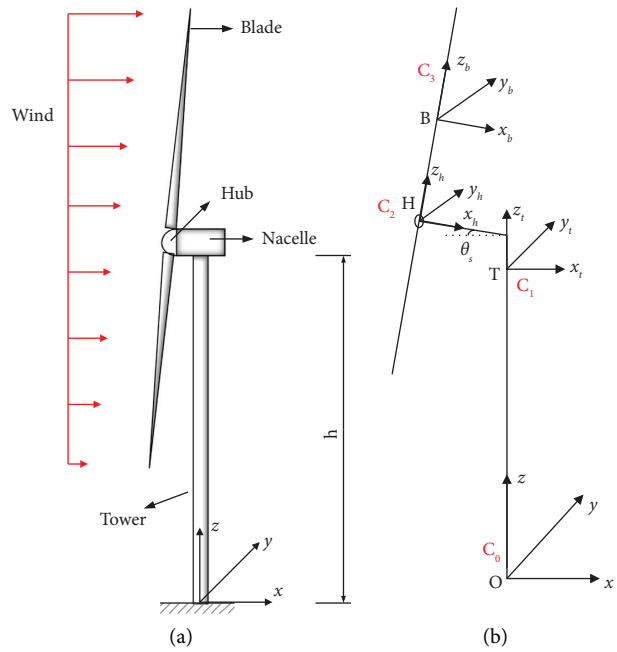

FIGURE 1: Simplified wind turbine model and coordinate systems. (a) Simplified model and global coordinate. (b) Local coordinate systems.

According to Reference [39], the transformation from tower-top system C_1 to global system C_0 is given as follows:

$$\vec{X}_1 = \vec{a}_{10}\vec{X}_0 + \vec{r}_{10} = \begin{bmatrix} 1 & 0 & 0 \\ 0 & 1 & 0 \\ 0 & 0 & 1 \end{bmatrix} \vec{X}_0 + (0, 0, h), \tag{2}$$

where h is the height of the tower.

The transformation from hub system C_2 to tower-top system C_1 is given as follows:

$$\vec{X}_2 = \vec{a}_{21}\vec{X}_1 + \vec{r}_{21} = \begin{bmatrix} \cos\theta_s & 0 & -\sin\theta_s \\ 0 & 1 & 0 \\ \sin\theta_s & 0 & \cos\theta_s \end{bmatrix} \vec{X}_1 + (-x_{\text{hub}}, 0, z_{\text{hub}}), \tag{3}$$

where θ_s represents the tilted angle of the shaft, x_{hub} is the distance between the hub center and z-axis, and z_{hub} is the vertical distance between the hub center and the tower-top base plate.

The transformation from blade system C_3 to hub system C_2 is given as follows:

$$\vec{X}_3 = \vec{a}_{32}\vec{X}_2 + \vec{r}_{32} = \begin{bmatrix} 1 & 0 & 0 \\ 0 & \cos\varphi & \sin\varphi \\ 0 & -\sin\varphi & \cos\varphi \end{bmatrix} \vec{X}_2 + (0, 0, R_{\text{hub}} + r), \tag{4}$$

where the azimuth angle φ is the angle between y_h and y_b, R_{hub} and r denote the radius of hub and the distance from blade cross-section to the blade root, respectively.

The motion of the wind turbine can be simplified by 8 degrees of freedom. Figure 2 illustrates the generalized coordinates of the tower-top base plate and blades. In Figure 2, parameters q_{ed1}~q_{ed3} and q_{fp1}~q_{fp3} denote the edgewise and flapwise tip displacement of the three blades, respectively. Parameters q_{fa} and q_{ss} denote the tower-top base plate displacement in the fore-aft (FA) and side-side (SS) directions. The detailed information is provided in Appendix A. Hence, the 8 degrees of freedom of a wind turbine can be defined by

$$\mathbf{q} = [q_1 \ \cdots \ q_8]^{\mathrm{T}} = [q_{ed1} \ q_{ed2} \ q_{ed3} \ q_{fp1} \ q_{fp2} \ q_{fp3} \ q_{fa} \ q_{ss}]^{\mathrm{T}}. \tag{5}$$

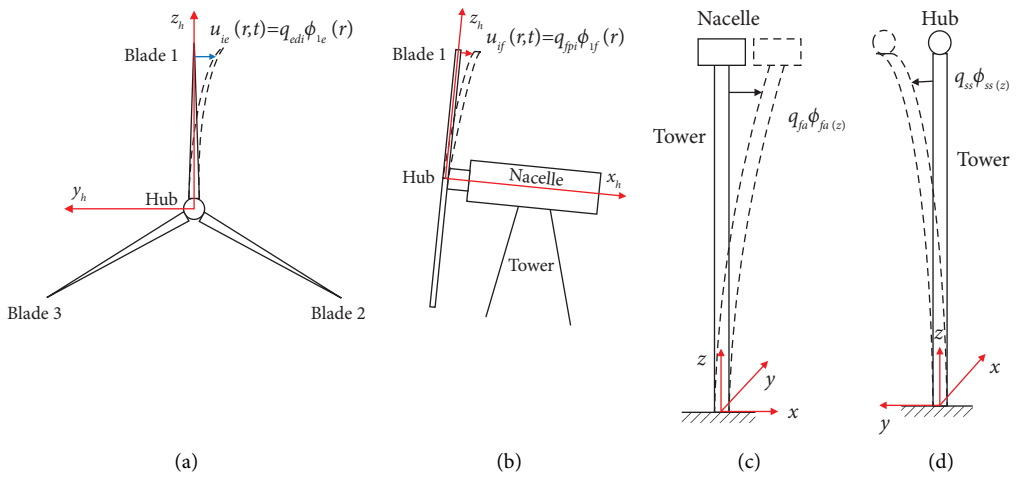

FIGURE 2: Diagrams of wind turbine components. (a) Edgewise vibration. (b) Flapwise vibration. (c) Fore-aft bending. (d) Side-side bending.

By defining the blade rotating speed $\Omega(t)$, the azimuth angle of the *ith* blade can be given as follows:

$$\varphi_i = \int_0^t \Omega(t)\mathrm{d}t + \frac{2\pi}{3}(i-1), \quad i = 1,2,3. \tag{6}$$

2.1.2. Tower Modeling. As described above, the absolute tower displacement can be expressed as follows:

$$\vec{u}_t(z,t) = q_{fa}\phi_{fa}(z)\vec{x} + q_{ss}\phi_{ss}(z)\vec{y}, \tag{7}$$

where $\phi_{fa}(z)$ and $\phi_{ss}(z)$ are the fundamental mode shape of the tower in the fore-aft and side-side directions, respectively.

In terms of equation (7), the kinetic energy of the tower is

$$T_t = \frac{1}{2}\int_0^h \overline{M}(z)\left(\vec{u}_t(z,t)\right)^2\mathrm{d}z = \frac{1}{2}\int_0^h \overline{M}(z)\left[\left(\dot{q}_{fa}\phi_{fa}(z)\right)^2 + \left(\dot{q}_{ss}\phi_{ss}(z)\right)^2\right]\mathrm{d}z, \tag{8}$$

where $\overline{M}(z)$ is the mass density per unit length of the tower.

In terms of Reference [37], the potential energy of the tower associated with the distributed stiffness and gravity is obtained by

$$V_t = \frac{1}{2}\int_0^h EI_t(z)\left[\left(\frac{\mathrm{d}^2\phi_{fa}(z)}{\mathrm{d}z^2}\right)^2 q_{fa}^2 + \left(\frac{\mathrm{d}^2\phi_{ss}(z)}{\mathrm{d}z^2}\right)^2 q_{ss}^2\right]\mathrm{d}z - g\left[\int_0^h \overline{M}(z)w(z,t)\mathrm{d}z\right], \tag{9}$$

where $EI_t(z)$ and $w(z,t)$ denote the distributed stiffness and the axial deflection at the height z of the tower, respectively. g is the acceleration of gravity. $w(z,t)$ can be expressed as follows:

$$w(z,t) = \frac{1}{2}\int_0^z \left[\frac{\partial \vec{u}_t(z',t)}{\partial z'}\right]^2 \mathrm{d}z', \tag{10}$$

where z' denotes the dummy variable along the tower height.

2.1.3. Nacelle and Hub Modeling. With the small deflection assumption of the tower and blades [37], the tower-top rotations θ_{fa} and θ_{ss} in both the fore-aft and side-side directions can be approximated:

$$\begin{aligned}\theta_{fa} &= \left.\frac{\mathrm{d}\phi_{fa}(z)}{\mathrm{d}z}\right|_{z=h} q_{fa},\\ \theta_{ss} &= \left.\frac{\mathrm{d}\phi_{ss}(z)}{\mathrm{d}z}\right|_{z=h} q_{ss}.\end{aligned} \tag{11}$$

Considering the additional displacement due to the tower-top rotations, the absolute displacement of the nacelle can be expressed as follows:

$$\vec{u}_n = \left(q_{fa} + \theta_{fa}z_{\mathrm{nac}}\right)\vec{x} + \left(q_{ss} + \theta_{ss}z_{\mathrm{nac}}\right)\vec{y} + \theta_{fa}x_{\mathrm{nac}}\vec{z}, \tag{12}$$

where z_{nac} is the vertical distance between the nacelle gravity center and the tower-top base plate, x_{nac} is the distance between the nacelle gravity center and z-axis.

Same as above, the absolute displacement of the hub can be expressed as follows:

$$\vec{u}_h = \left(q_{fa} + \theta_{fa}z_{\mathrm{hub}}\right)\vec{x} + \left(q_{ss} + \theta_{ss}z_{\mathrm{hub}}\right)\vec{y} + \theta_{fa}x_{\mathrm{hub}}\vec{z}. \tag{13}$$

The total kinetic energy of the nacelle and hub is

$$T_{nh} = \frac{1}{2}M_n\left(\vec{u}_n\right)^2 + \frac{1}{2}M_h\left(\vec{u}_h\right)^2. \tag{14}$$

The total potential energy of the nacelle and hub is

$$V_{nh} = -g(M_n + M_h)w(h,t), \tag{15}$$

where M_n and M_h denote the mass of the nacelle and hub, respectively.

2.1.4. Blade Modeling. As shown in Figure 2, parameters $u_{ie}(r,t)$ and $u_{if}(r,t)$ denote the edgewise and flapwise deflections of blade cross-section at a distance r from the blade root, following as

$$u_{ie}(r,t) = q_{\text{edi}}\phi_{1e}(r), u_{if}(r,t) = q_{\text{fpi}}\phi_{1f}(r), \quad i = 1,2,3, \tag{16}$$

where $\phi_{1e}(r)$ and $\phi_{1f}(r)$ represent the edgewise and flapwise fundamental mode shape, respectively.

At a distance r from the blade root, the displacement of blade can be expressed as follows:

$$\vec{u}_{1bi}(r,t) = q_{fpi}\phi_{1f}(r)\vec{x}_b - q_{\text{edi}}\phi_{1e}(r)\vec{y}_b, \quad i = 1,2,3. \tag{17}$$

Then, the displacement of blade in the global coordinate system C_0 can be given as follows:

$$\begin{aligned}\vec{u}_{bi}(r,t) = {} & (\vec{a}_{10})^{-1}(\vec{a}_{21})^{-1}(\vec{a}_{32})^{-1}\vec{u}_{1bi}(r,t) + \vec{u}_t(h,t) \\ & + (\vec{a}_{10})^{-1}\vec{\theta} \times \left[(\vec{a}_{10})^{-1}\overrightarrow{TH} + (\vec{a}_{10})^{-1}(\vec{a}_{21})^{-1}(\vec{a}_{32})^{-1}\overrightarrow{HB}\right], \quad i = 1,2,3,\end{aligned} \tag{18}$$

where $\vec{\theta}$ is the tower-top rotation due to the bending of the tower, $\overrightarrow{TH}$ denotes the vector between the origins of coordinate system C_1 and C_2, and $\overrightarrow{HB}$ represents the vector between the origins of coordinate system C_2 and C_3. They can be expressed as follows:

$$\begin{aligned}\vec{\theta} &= -\theta_{ss}\vec{x}_t + \theta_{fa}\vec{y}_t, \\ \overrightarrow{TH} &= -x_{\text{hub}}\vec{x}_t + z_{\text{hub}}\vec{z}_t, \\ \overrightarrow{HB} &= (R_{\text{hub}} + r)\vec{z}_b.\end{aligned} \tag{19}$$

The kinetic energy of the blades can be expressed as follows:

$$T_b = \frac{1}{2}\sum_{i=1}^{3}\int_0^R m(r)\left(\dot{\vec{u}}_{bi}(r,t)\right)^2 \mathrm{d}r, \tag{20}$$

where $m(r)$ is the mass density per unit length of the blades, and R denotes the distance from the blade tip to the root.

The potential energy is obtained by considering the strain energy of the blades due to the bending, the additional strain energy owing to the gravity, and the centrifugal stiffening effect. In terms of Reference [39], the total potential energy of blades can be obtained by

$$\begin{aligned}V_b = {} & \sum_{i=1}^{3}\frac{1}{2}\int_0^R EI_{eg}(r)\left(\frac{\mathrm{d}^2\phi_{1e}(r)}{\mathrm{d}r^2}q_{\text{edi}}\right)^2\mathrm{d}r + \sum_{i=1}^{3}\frac{1}{2}\int_0^R EI_{fp}(r)\left(\frac{\mathrm{d}^2\phi_{1f}(r)}{\mathrm{d}r^2}q_{\text{fpi}}\right)^2\mathrm{d}r \\ & - \frac{1}{2}\sum_{i=1}^{3}\int_0^R m(r')g\left\{\left[\int_0^{r'}\left(\frac{\mathrm{d}\phi_{1e}(r)}{\mathrm{d}r}q_{\text{edi}}\right)^2\mathrm{d}r\right] + \left[\int_0^{r'}\left(\frac{\mathrm{d}\phi_{1f}(r)}{\mathrm{d}r}q_{\text{fpi}}\right)^2\mathrm{d}r\right]\right\}\cos\varphi_i\mathrm{d}r' \\ & + \sum_{i=1}^{3}\frac{1}{2}\int_0^R m(r')\Omega(t)^2(R_{\text{hub}} + r')\left\{\left[\int_0^{r'}\left(\frac{\mathrm{d}\phi_{1e}(r)}{\mathrm{d}r}q_{\text{edi}}\right)^2\mathrm{d}r\right] + \left[\int_0^{r'}\left(\frac{\mathrm{d}\phi_{1f}(r)}{\mathrm{d}r}q_{\text{fpi}}\right)^2\mathrm{d}r\right]\right\}\mathrm{d}r',\end{aligned} \tag{21}$$

where $EI_{eg}(r)$ and $EI_{fp}(r)$ denote the edgewise bending stiffness and the flapwise bending stiffness, respectively. r' represents the dummy variable along the blade length.

2.2. The Aerodynamic Model

2.2.1. The Wind Turbulence Model. Wind speed can be expressed as the combination of the mean and fluctuating components, $v(z,t) = \overline{v}(z) + \tilde{v}(z,t)$, the exponential wind profile is adopted to calculate the mean speed:

$$\overline{v}(z) = \overline{v}_{\text{Hub}}\left(\frac{z}{z_{\text{Hub}}}\right)^{\alpha_0}, \tag{22}$$

where $\overline{v}_{\text{Hub}}$ represents the mean wind speed at the height of the hub, z_{Hub} and α_0 denote the height of the hub and wind shear exponent, respectively.

The fluctuating component is computed using the IEC Kaimal spectral model [32]. The spatial correlation between two points in space is determined by the coherent function in IEC61400-1 [40].

Based on the above theory, a three-dimensional wind field profile covering the domain of the rotor disk and tower is generated using the TurbSim [41] program. The wind field is sampled in real time, and bilinear interpolation is used to obtain wind speeds on the blades and tower using the developed MATLAB code.

2.2.2. Aerodynamic Loading. The aerodynamic loading of the wind turbine consists of the rotating blades and the tower. The aerodynamic loading of the tower is calculated by quasi-steady theory [42]. The aerodynamic loading per unit length of tower can be expressed as follows:

$$F_t(z,t) = \frac{1}{2}\rho C_{dt} d_t(z)\left[v(z,t) - \dot{q}_{fa}(t)\phi_{fa}(z)\right]^2, \quad (23)$$

where ρ is the air density, and C_{dt} and $d_t(z)$ denote the drag coefficient and the outside diameter of the tower section, respectively.

Under $F_t(z,t)$, the virtual work done by external wind load is

$$\delta W_t = \int_0^h F_t(z,t)\phi_{fa}(z)\delta q_{fa}\mathrm{d}z. \quad (24)$$

The aerodynamic loading acting on the rotating blades can be calculated by applying the blade element momentum theory [31], eddy current theory [31], and computational fluid dynamics [43]. In the paper, the blade element momentum (BEM) theory is used to estimate the aerodynamic loading, neglecting unsteady indicial variation and the dynamics of vorticity shed. The BEM is a combination of momentum theory and blade element theory. It is assumed that there is no radial interaction, which means that the aerodynamic force at one element cannot be influenced by the others. It is assumed that the forces on a blade element can be calculated by means of two-dimensional airfoil characteristics under an angle of attack, ignoring three-dimensional effects. Considering the aeroelasticity of the wind turbine, the blade velocities are returned to the BEM theory so that the aerodynamic loads are estimated based on the relative velocities. Therefore, the time series of the aerodynamic loading can be calculated from the blade characteristics, blade velocity, and wind speed. The blade characteristics consist of the number of blades, pretwist, chord distribution, airfoils, and pitch angle. Figure 3 illustrates the blade element of wind turbines for BEM analysis.

Figure 4 shows all the velocities and forces relative to the blade chord line at radius r from the blade root. From Figure 4, the resultant relative velocity at the blade is

$$v_{\mathrm{rel}}(r,t) = \sqrt{(vb - \dot{u}_{\mathrm{bxi}})^2(1-a)^2 + \left(-\dot{u}_{\mathrm{byi}}\right)^2\left(1+a'\right)^2}, \quad (25)$$

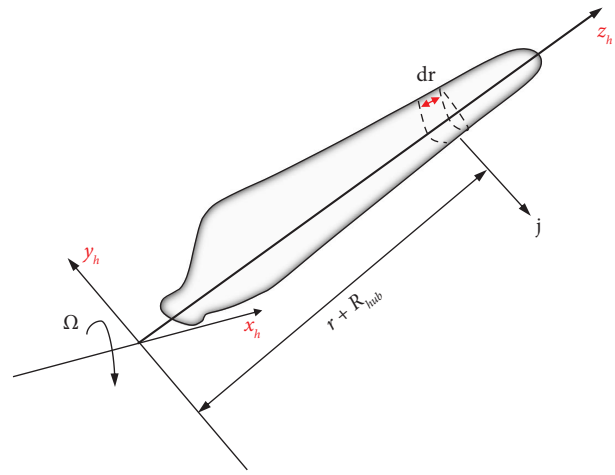

Figure 3: Blade element for BEM analysis.

where vb represents the wind speed in the blade coordinate system, $\dot{u}_{\mathrm{bxi}}$ and $\dot{u}_{\mathrm{byi}}$ denote the velocity components of the blade cross-section at a distance r from the blade root in the blade coordinate system. a and a' are the axial and tangential induction factors, respectively. In general, a and a' are unknown and obtained by iterations.

The flow angle ψ to the plane of rotation can be calculated by

$$\sin\psi = \frac{(vb - \dot{u}_{\mathrm{bxi}})(1-a)}{v_{\mathrm{rel}}}. \quad (26)$$

The angle of attack α is given by

$$\alpha = \psi - \beta - \gamma, \quad (27)$$

where β is the pitch angle, and γ is the twist angle which is determined by the airfoil.

In terms of the attack angle, the lift and drag coefficients C_l and C_d can be looked up by the airfoil data which is obtained by experiments [38]. On a span-wise length of each blade, the lift force is normal to the direction of the resultant relative velocity, and the drag force which is parallel to the resultant relative velocity can be expressed as follows:

$$L = C_l(\alpha) \times \frac{1}{2}\rho v_{\mathrm{rel}}^2 c,$$
$$D = C_d(\alpha) \times \frac{1}{2}\rho v_{\mathrm{rel}}^2 c, \quad (28)$$

where c is the chord length.

The normal forces P_N and the tangential forces P_T can be computed as follows:

$$P_N = L\cos\psi + D\sin\psi,$$
$$P_T = L\sin\psi - D\cos\psi. \quad (29)$$

The aerodynamic loadings acting on the rotating blades can be calculated by equations (25)–(29) via BEM. In order to obtain better results, it is necessary to apply two corrections to the BEM. Both Prandtl's tip loss factor and Glauert correction are considered in this study, and the

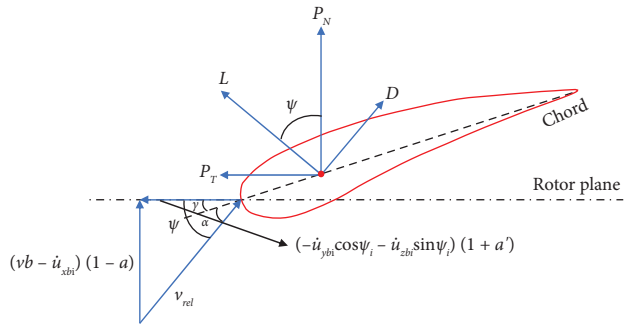

FIGURE 4: Velocity and force distribution on blade cross-section.

related theories can be found in literature [39]. Then the virtual work done by P_N and P_T can be computed by:

$$\delta W_b = \sum_{i=1}^{3}\int_0^R P_{Ni}(r,t)\delta u_{\text{xbi}}dr + \sum_{i=1}^{3}\int_0^R P_{Ti}(r,t)\delta\left(-u_{\text{ybi}}\cos\varphi_i - u_{\text{zbi}}\sin\varphi_i\right)\text{d}r. \tag{30}$$

Hence, the virtual work done by aerodynamic loadings can be expressed as follows:

$$\delta W = \delta W_t + \delta W_b. \tag{31}$$

In terms of the principles of work and energy, the generalized force can be determined as follows:

$$Q_{i,\text{wind}} = \frac{\partial(\delta W)}{\partial(\delta q_i)}. \tag{32}$$

Substituting expression of the equation (31) into equation (32), the generalized force can be provided by

$$\begin{aligned}
Q_{i,\text{wind}} &= \int_0^R P_{Ti}(r,t)\phi_{1e}(r)\text{d}r, Q_{i+3,\text{wind}} = \int_0^R P_{Ni}(r,t)\phi_{1f}(r)\text{d}r, \quad i = 1,2,3,\\
Q_{7,\text{wind}} &= \int_0^h F_t(z,t)\phi_{fa}(z)\text{d}z\\
&\quad + \sum_{i=1}^{3}\int_0^R P_{Ni}(r,t)\left(\cos\theta_s + ((r+R_{\text{hub}})\cos\varphi_i - x_{\text{hub}}\sin\theta_s + z_{\text{hub}}\cos\theta_s)\frac{\text{d}\phi_{fa}(z)}{\text{d}z}\Big|_{z=h}\right)\text{d}r\\
&\quad - \sum_{i=1}^{3}\int_0^R P_{Ti}(r,t)\left(\sin\theta_s\sin\varphi_i + (x_{\text{hub}}\sin\varphi_i\cos\theta_s + z_{\text{hub}}\sin\varphi_i\sin\theta_s)\frac{\text{d}\phi_{fa}(z)}{\text{d}z}\Big|_{z=h}\right)\text{d}r,\\
Q_{8,\text{wind}} &= -\sum_{i=1}^{3}\int_0^R P_{Ni}(r,t)\left((r+R_{\text{hub}})\sin\varphi_i\sin\theta_s\frac{\text{d}\phi_{ss}(z)}{\text{d}z}\Big|_{z=h}\right)\text{d}r\\
&\quad - \sum_{i=1}^{3}\int_0^R P_{Ti}(r,t)\left(\cos\varphi_i + ((r+R_{\text{hub}})\cos\theta_s + z_{\text{hub}}\cos\varphi_i)\frac{\text{d}\phi_{ss}(z)}{\text{d}z}\Big|_{z=h}\right)\text{d}r.
\end{aligned} \tag{33}$$

2.3. The Servo System. The servo system of the wind turbine includes a generator-torque controller and a full-span rotor-collective blade-pitch controller [38]. The flowchart of the whole servo control system is shown in Figure 5.

According to Reference [38], the dynamic model of the drivetrain can be obtained as follows:

$$\left(J_r + N_g^2 J_g\right)\dot{\Omega}(t) = T_{\text{aero}} - N_g M_g. \tag{34}$$

The generator torque versus generator speed response curve is adopted by the generator-torque controller. With proportional-integral (PI) control, the control law of pitch angle is

$$\theta_p(t) = K_P N_g \Delta\Omega + K_I\int_0^t N_g\Delta\Omega\text{d}t. \tag{35}$$

In terms of the kinetic energy and potential energy of wind turbines, the generalized force, the servo system, and the Euler–Lagrange equation, the motion of wind turbine can be computed as follows:

$$\mathbf{M}\ddot{\mathbf{q}} + \mathbf{K}\mathbf{q} + \mathbf{C}\dot{\mathbf{q}} = \mathbf{Q}_{\text{wind}}, \tag{36}$$

where the structural damping of the blade and tower adopts Rayleigh damping, which is directly added to the C matrix. The detailed information on matrices is provided in Appendix B.

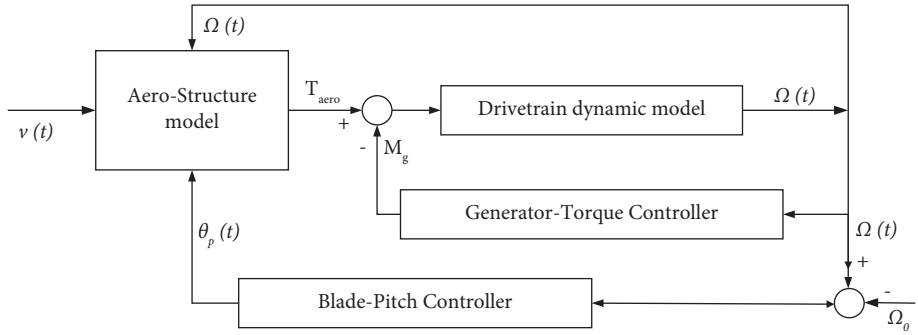

Figure 5: Flowchart of the servo system.

Based on the aerodynamic module, structure module, and servo system module, the holistic coupled ASSC model is established on MATLAB/Simulink, which can be seen in Figure 6. Also, Table 1 shows the detailed information of the developed ASSC model.

3. Verification and Analysis of the ASSC Model

First, the natural frequencies of the 5 MW onshore wind turbine structure are compared by using the ASSC model and FAST. Then, the dynamic responses of wind turbine under the ASSC model and FAST model are analyzed, and the accuracy and effectiveness of the ASSC model are evaluated. The vibration at the tower top in the fore-aft direction is the largest for the tower, and its control is focused. Consequently, it mainly verifies and analyzes the fore-aft response of the wind turbine. As shown in Table 2, the 5 MW onshore wind turbine given by NREL is summarized.

3.1. Comparison of Natural Frequencies. The natural frequencies of the wind turbine in FAST are determined by the linearization module at the initial moment. The frequencies of the ASSC model are also obtained at the same time by the eigenvalue analysis of equation (36). Then, the results of the ASSC model and FAST are compared in Table 3. It can be seen from the table that the ASSC model can predict the natural frequencies of wind turbine well, with an error of less than 3%.

3.2. Comparison of Responses in Turbulent Winds. The dynamic responses of the ASSC and FAST models under turbulent winds are analyzed and compared. Three typical conditions are considered in this paper: Case 1: the mean wind speed is 30 m/s at parked condition; Case 2: the mean wind speed is 8 m/s at operational condition; and Case 3: the mean wind speed is 16 m/s at operational condition. The turbulence intensities (TI) for these conditions are 0.18.

The time histories and power spectra under these conditions are shown in Figures 7–9. It can be seen that the structural responses of the ASSC model and FAST are in good agreement both in the time and frequency domain. The tower response is dominated by the fundamental frequency (0.322 Hz) at parked condition, as shown in Figure 7. Figures 8 and 9 show the tower top responses with the wind speed of 8 m/s and 16 m/s at operational conditions, respectively. The following observations can be found. The tower fundamental frequency, 3P frequency, and 6P frequency can be observed in tower top FA responses. Note that the 3P frequency is three times the rotor rotation frequency. At operational condition, the tower displacement is dominated by the tower fundamental frequency, while the acceleration is dominated by the 3P frequency. Compared with the parked condition, the tower fundamental frequencies at wind speeds of 8 m/s and 16 m/s have changed to 0.337 Hz and 0.347 Hz, respectively. It is indicated in Figures 8(c) and 8(d) that the 3P frequency is not constant and exists in a wide frequency band, which is due to the fact that the rotor speed is not constant. However, as shown in Figures 9(c) and 9(d), the 3P frequency is constant at 0.61 Hz, which is due to the fact that the blade-pitch angle changes in real time to keep the rotational speed constant.

Clearly, during normal operational conditions, the aerodynamic loads and structural characteristics of wind turbines will change at different wind speeds due to the existence of the servo control system. As a result, it can be concluded that the developed ASSC model has good precision and accuracy at both parked and operational conditions, which can be used to calculate the structural responses of the wind turbine.

4. Control by ATMD Using the ASSC Model

4.1. Wind Turbine-ATMD Control Model. From Figure 10, it is seen that ATMD is installed at the top of the tower to reduce tower vibration in the fore-aft direction. Compared with the 8 degrees of freedom of the uncontrolled model, the displacement and speed of ATMD need to be considered. Therefore, the wind turbine-ATMD controlled model has nine degrees of freedom. On the basis of the developed ASSC model, the motion equation of the wind turbine-ATMD controlled model needs to be rededuced. The new equation of motion is as follows:

$$\mathbf{M_1}\ddot{\mathbf{y}} + \mathbf{K_1}\mathbf{y} + \mathbf{C_1}\dot{\mathbf{y}} = \mathbf{Q_{wind1}} + \mathbf{U},$$
$$\mathbf{y} = \begin{bmatrix} \mathbf{q} \\ x_{\mathrm{ATMD}}(t) \end{bmatrix}, \tag{37}$$

where $\mathbf{M}_1$, $\mathbf{K}_1$, $\mathbf{C}_1$, and $\mathbf{Q}_1$ are the derived mass, stiffness, damping, and load matrices after adding ATMD, the detailed information on matrices are provided in Appendix C,

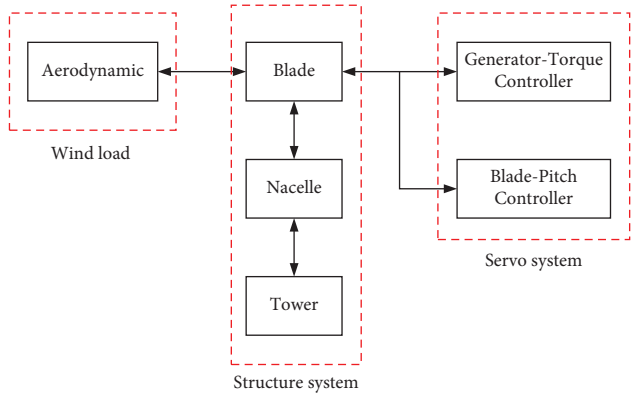

Figure 6: Diagram of the ASSC model.

Table 1: The detail information of the developed ASSC model.

Aerodynamic module	Wind turbulence model	Obtained from TurbSim [41]
	Aerodynamic loading	Developed in Simulink
Structure module	Blade, nacelle, and tower	Developed in Simulink
Servo system module	Generator-torque controller	Established in Simulink [38]
	Blade-pitch controller	Established in Simulink [38]

Table 2: Parameters of the NREL 5-MW baseline wind turbine.

Gross properties	Rating	5 MW
	Rotor diameter	126 m
	Hub height	90 m
	Cut-in, rated, cut-out wind speed	3 m/s, 11.4 m/s, 25 m/s
	Cut-in, rated rotor speed	6.9 rpm, 12.1 rpm
Blade	Length	61.5 m
	Mass	17,740 kg
	Second moment of inertia	11,776 kg m^2
	1st mode damping ratio (edgewise and flapwise)	0.48%
Nacelle + hub	Nacelle mass	240,000 kg
	Hub mass	56,780 kg
	Hub diameter	3 m
	Hub height above ground	90 m
Tower	Height above ground	87.6 m
	Overall (integrated) mass	267,650 kg
	1st fore-aft (side-side) modal damping ratio	1%

Table 3: Frequencies comparison between the ASSC model and FAST.

	Tower fore-aft (Hz)	Tower side-side (Hz)	Blade1 flapwise (Hz)	Blade2 flapwise (Hz)	Blade3 flapwise (Hz)	Blade1 edgewise (Hz)	Blade2 edgewise (Hz)	Blade3 edgewise (Hz)
ASSC model	0.3278	0.3189	0.7154	0.7011	0.6984	1.1516	1.1226	1.1218
FAST	0.3341	0.3148	0.7251	0.7186	0.7167	1.1372	1.1011	1.1002
Error	1.89%	1.30%	1.34%	2.44%	2.55%	1.27%	1.95%	1.96%

respectively. $x_{\mathrm{ATMD}}(t)$ is the relative displacement of ATMD device to the top of the tower. $\mathbf{U}$ is the generalized active control force vector of ATMD, expressed as follows:

$$\mathbf{U} = \mathbf{B}u_a, \tag{38}$$

where the control influence matrix, $\mathbf{B}$ is given by

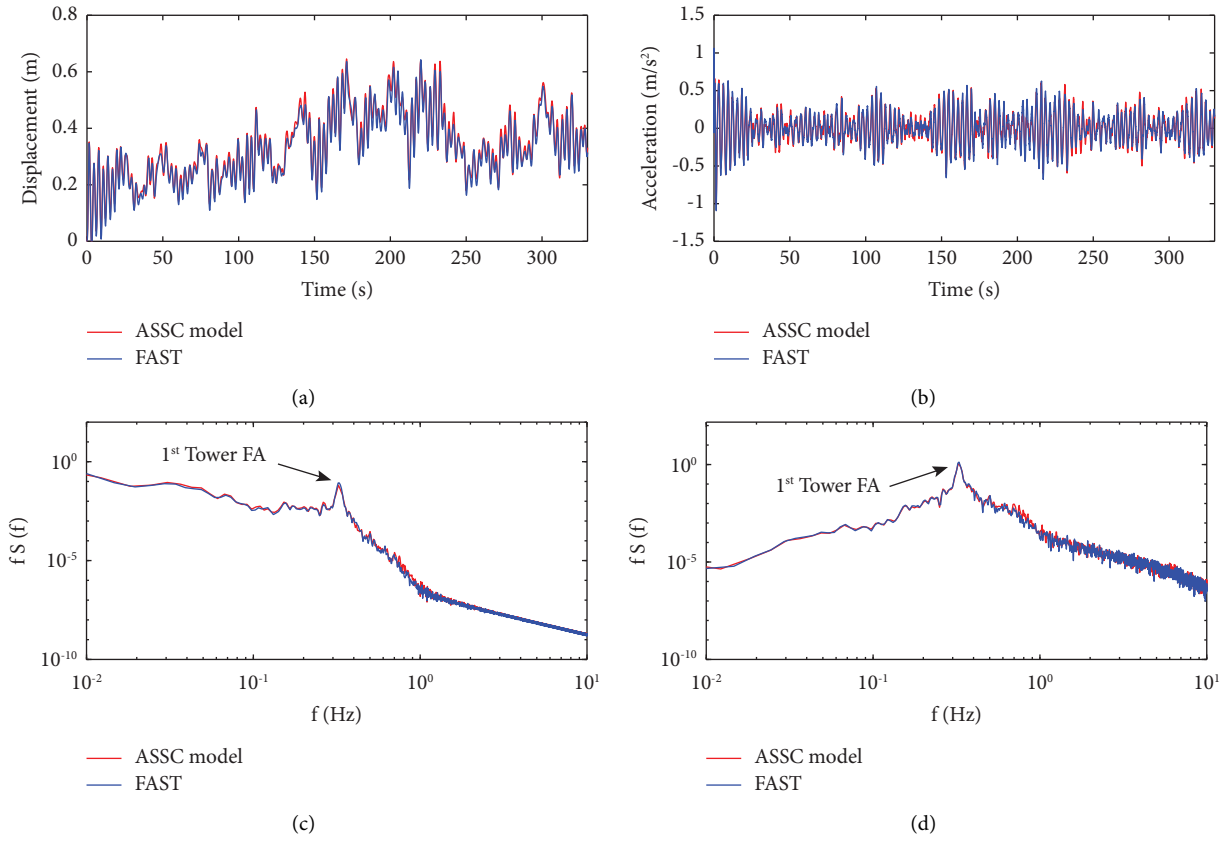

FIGURE 7: Tower-top FA responses under turbulent wind (park at $\bar{v}_{\text{Hub}} = 30\,m/s, TI = 0.18$). (a) Displacement time history. (b) Acceleration time history. (c) Displacement PSD. (d) Acceleration PSD.

$$\mathbf{B}^{\text{T}} = [0\ 0\ 0\ 0\ 0\ 0\ 1\ 0\ -1], \tag{39}$$

where u_a is the active control force of ATMD.

The new equation of motion is rewritten into a state-space equation and the new state variable is

$$\mathbf{X} = \begin{bmatrix} \mathbf{q} \\ x_{\text{ATMD}}(t) \\ \dot{\mathbf{q}} \\ \dot{x}_{\text{ATMD}}(t) \end{bmatrix}. \tag{40}$$

The new state space equation is

$$\dot{\mathbf{X}} = \mathbf{A}_{\mathbf{S}}\mathbf{X} + \mathbf{B}_{\mathbf{Q}}\mathbf{Q}_{\text{wind1}} + \mathbf{B}_{\mathbf{U}}\mathbf{U}, \tag{41}$$

where, $\mathbf{A}_{\mathbf{S}} = \begin{bmatrix} \mathbf{0}_{9\times9} & \mathbf{I}_{9\times9} \\ -\mathbf{M}_1^{-1}\mathbf{K}_1 & -\mathbf{M}_1^{-1}\mathbf{C}_1 \end{bmatrix}$, $\mathbf{B}_{\mathbf{Q}} = \begin{bmatrix} \mathbf{0}_{9\times1} \\ \mathbf{M}_1^{-1} \end{bmatrix}$, $\mathbf{B}_{\mathbf{U}} = \begin{bmatrix} \mathbf{0}_{9\times1} \\ \mathbf{M}_1^{-1} \end{bmatrix}$.

4.2. Active Control Algorithm Based on the Virtual TMD System. The proposed active control algorithm based on the virtual TMD system is presented in this subsection. As shown in Section 3, the vibration of a wind turbine tower is dominated by the tower fundamental frequency and 3P frequency at operational condition. Therefore, a control scheme with a wide effective bandwidth is required to achieve the vibration reduction of wind turbine. When the TMD mass ratio is large enough (e.g., 15%~30%), it is expected to meet the requirements of wide-band vibration reduction. With this inspiration, the performance and mechanism of vibration reduction for the TMD with a mass ratio of 20% are analyzed firstly. Then, the control force of the TMD with a large mass ratio is applied to wind turbines by an ATMD with a mass ratio of 2% to achieve the same reduction effect as the TMD with a large mass ratio. Finally, the parameters of virtual TMD are optimized to improve the control effect of ATMD.

4.2.1. Control Effect of TMD with Large Mass Ratio and Damping Ratio. Figure 11 shows the power spectral density (PSD) function of tower top acceleration at operational condition and frequency response functions under uncontrolled and three controlled cases. These controlled conditions are: Case 1, the mass ratio of the TMD is 2%, the damping ratio is 9%, and the tuning frequency is the fundamental frequency; Case 2, the mass ratio of the TMD is 2%, the damping ratio is 9%, and the tuning frequency is the 3P frequency; Case 3, the mass ratio of the TMD is 20%, the damping ratio is 25%, and the tuning frequency is the 3P frequency. It is seen that the tower-top acceleration response is dominated by the 3P frequency. The fundamental tower frequency is also observed in tower top acceleration.

For Case 1, the response amplitude at the fundamental frequency is significantly reduced, and that at 3P almost does not change, compared with those of the uncontrolled case. For Case 2, although the tuning frequency of TMD changes

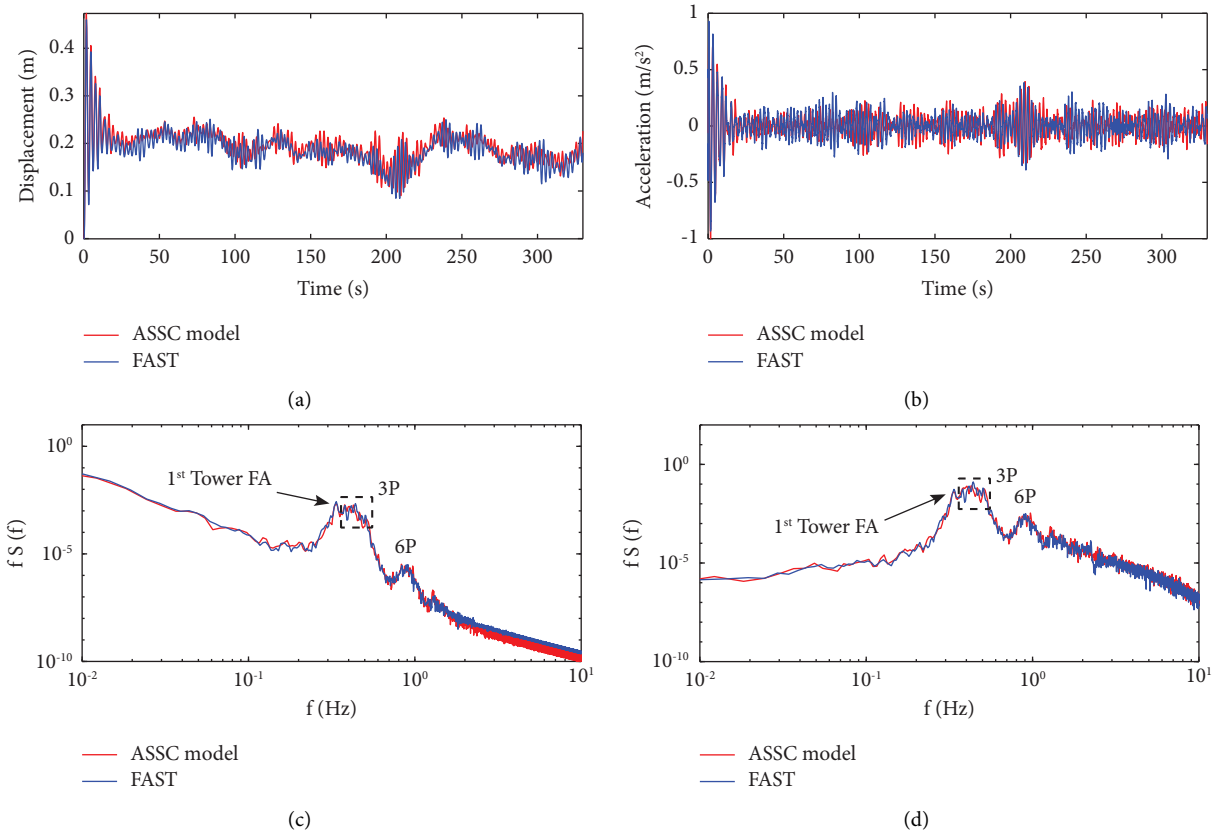

FIGURE 8: Tower-top FA responses under turbulent wind (operation at $\bar{v}_{\text{Hub}} = 8\,m/s$, $TI = 0.18$). (a) Displacement time history. (b) Acceleration time history. (c) Displacement PSD. (d) Acceleration PSD.

to the 3P frequency, the amplitude at the 3P frequency does not change obviously compared with that of the uncontrolled case. It indicates that the response amplitude at the frequency far away from the natural frequency cannot be reduced by the traditional passive control like TMD. However, for Case 3, the amplitudes both at the fundamental frequency and 3P frequency have been significantly reduced by TMD with a large mass and damping ratio.

4.2.2. The Virtual TMD Algorithm for the ATMD Control. From the above, it indicates that TMD with a large mass ratio and damping ratio can significantly reduce the response of wind turbine. Although this type of TMD cannot be realized in the wind turbine, the concept of the virtual TMD with a large mass ratio and damping ratio can be used here. The active control force of the ATMD with 2% mass ratio can be obtained by the virtual TMD with a large mass ratio and damping ratio. Then, the ATMD can achieve the same control effect as the virtual TMD system. On this basis, an active control algorithm based on virtual TMD is proposed to mitigate tower vibration in the fore-aft direction.

In the proposed control algorithm, the motion equation of the virtual TMD system can be given as follows:

$$m_{v\text{TMD}}\left(\ddot{x}_s + \ddot{x}_{v\text{TMD}}\right) + k_{v\text{TMD}}x_{v\text{TMD}} + c_{v\text{TMD}}\dot{x}_{v\text{TMD}} = 0, \tag{42}$$

where $\ddot{x}_s$ and $\ddot{x}_{v\text{TMD}}$ represent the acceleration of the structure and the virtual TMD, respectively. $k_{v\text{TMD}}$ and $c_{v\text{TMD}}$ denote the stiffness and damping of the virtual TMD, respectively.

Then, the control force of the virtual TMD system can be expressed as follows:

$$F_{v\text{TMD}} = k_{v\text{TMD}}x_{v\text{TMD}} + c_{v\text{TMD}}\dot{x}_{v\text{TMD}}. \tag{43}$$

The ATMD system can be used to simulate the control force of the virtual TMD system. Then, the motion of the ATMD device can be expressed as follows:

$$F_{v\text{TMD}} = -m_{\text{TMD}}\left(\ddot{x}_s + \ddot{x}_{\text{TMD}}\right), \tag{44}$$

$$m_{\text{TMD}}\left(\ddot{x}_s + \ddot{x}_{\text{TMD}}\right) + k_{\text{TMD}}x_{\text{TMD}} + c_{\text{TMD}}\dot{x}_{\text{TMD}} + U = 0, \tag{45}$$

where k_{TMD} and c_{TMD} denote the stiffness and damping of the TMD, respectively. Also, $\ddot{x}_{\text{TMD}}$ represents the acceleration of the TMD.

The ATMD feedback control force is determined by the virtual TMD system. The active control force of ATMD can be obtained by equations (42)–(45). Then, the responses of the wind turbine at the 3P frequency can be significantly reduced. Figure 12 illustrates the diagram of Simulink for the virtual TMD algorithm. The algorithm has good robustness and broadband characteristics due to the large mass ratio of the

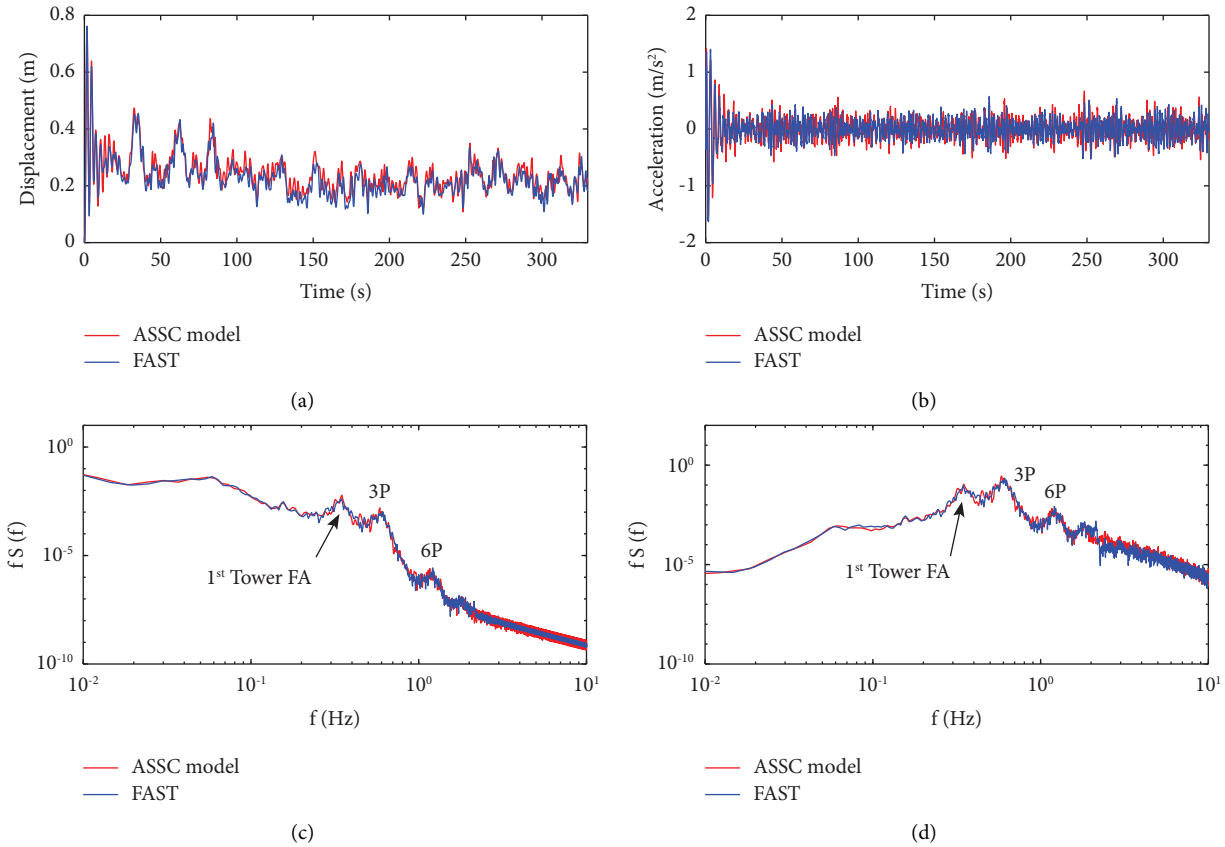

FIGURE 9: Tower-top FA responses under turbulent wind (operation at $\overline{v}_{\text{Hub}} = 16\,m/s$, $TI = 0.18$). (a) Displacement time history. (b) Acceleration time history. (c) Displacement PSD. (d) Acceleration PSD.

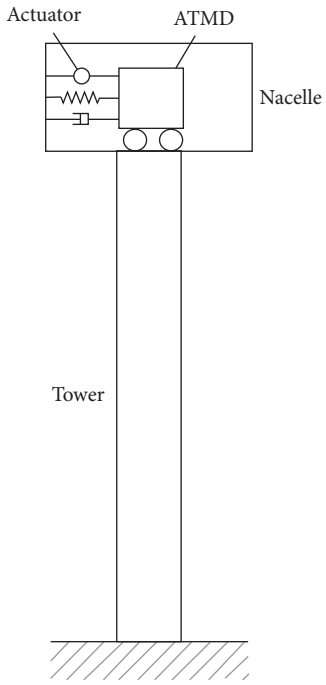

FIGURE 10: Diagram of wind turbine with the ATMD control.

virtual TMD. Furthermore, unlike the LQR control algorithm, the proposed control algorithm does not require the full states. The acquisition of sole requirement is to acquire either the acceleration information on the top of the tower or the relative displacement of the active TMD. This information can be conveniently obtained. Once the acceleration information is available, the acceleration $\ddot{x}_{\text{TMD}}$ of the active TMD can be determined by solving equations (42)–(44). Integrating the acceleration $\ddot{x}_{\text{TMD}}$ allows determination of the displacement x_{TMD} and velocity $\dot{x}_{\text{TMD}}$ of the active TMD. Then the active control force of the ATMD can be calculated by substituting x_{TMD}, $\dot{x}_{\text{TMD}}$ and $\ddot{x}_{\text{TMD}}$ into equation (45). Similarly, knowing the displacement of the active TMD enables obtaining the active control force of the ATMD by solving equations (42)–(45). Considering the impact of noise on the signal, we recommend obtaining the relative displacement information of the active TMD. Figure 13 illustrates the comparison of results between the pure virtual passive TMD and the ATMD using the virtual TMD algorithm under the same parameters. It can be seen from Figures 13(a) and 13(b) that the acceleration responses of the wind turbine and the control force of the two are almost the same. It indicates that the ATMD utilizing the virtual TMD algorithm can accurately replicates the control force of the pure virtual passive TMD and achieve the same control effect.

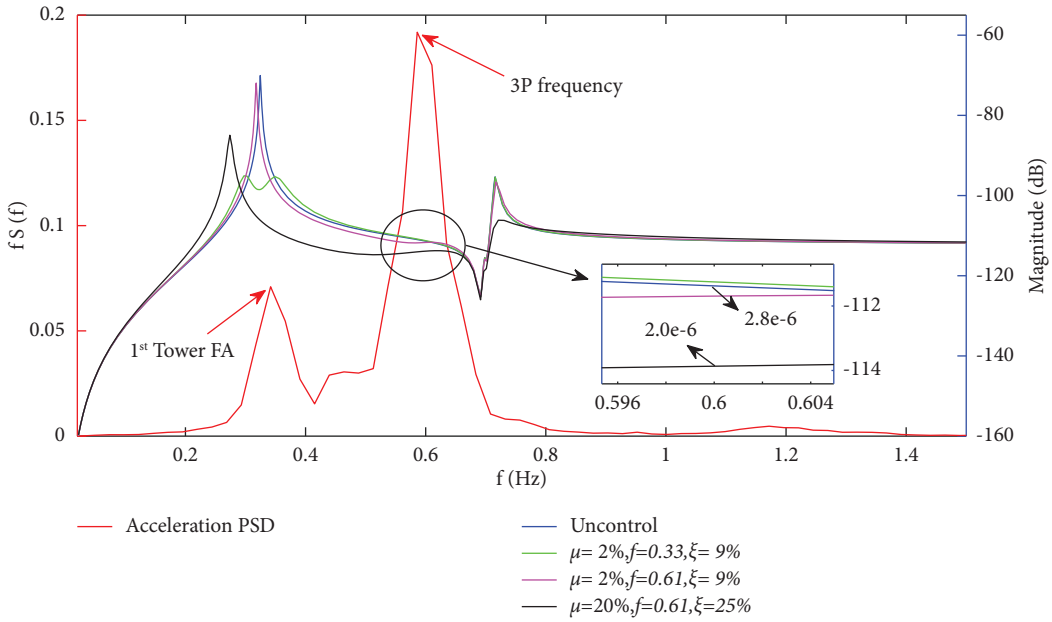

Figure 11: The power spectral density of acceleration and frequency response functions under different control cases.

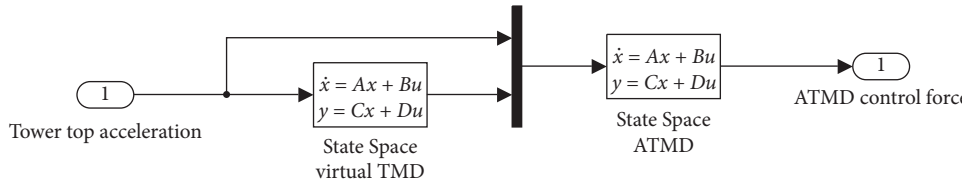

Figure 12: The Simulink diagram for the virtual TMD algorithm.

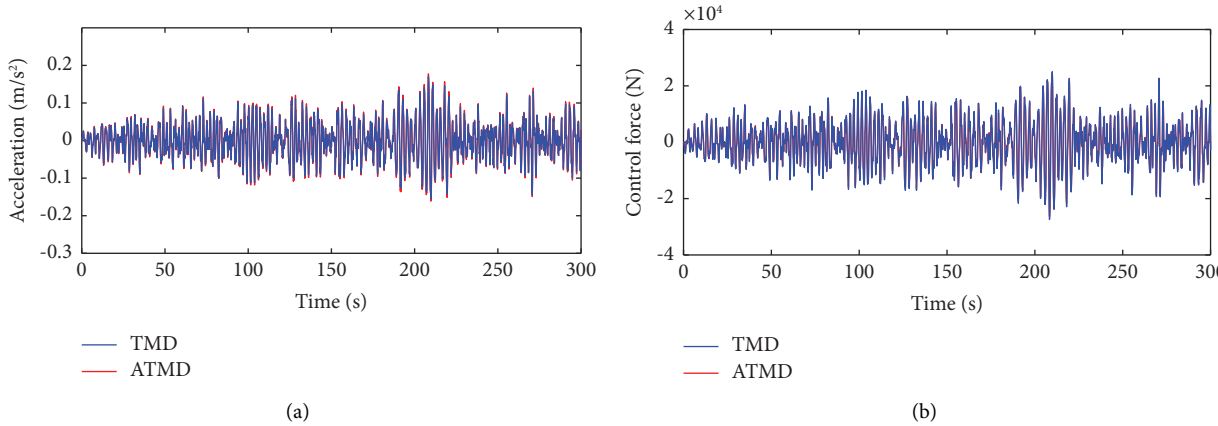

Figure 13: The tower-top acceleration responses and damper control forces between the pure virtual passive TMD and the ATMD using virtual TMD algorithm. (a) Time histories of acceleration. (b) Time histories of control force.

4.2.3. Optimal Design for the Virtual TMD Algorithm. In this paper, the proposed control algorithm is adopted to realize the vibration control of the wind turbines at parked and operational conditions. At parked conditions, the optimal frequency and damping ratio of the virtual TMD system can be obtained in the literature [44]. For operational conditions, a numerical search is adopted to obtain the optimal design. The acceleration RMS is set as the objective function. The optimal objective is to minimize the RMS of the tower-top acceleration.

The frequency ratio is defined as the ratio of the tuned frequency to the 3P frequency. With a given mass ratio, the value of the objective function corresponding to different frequency and damping ratio values are calculated. Figure 14 shows the value of the objective function against frequency and damping ratio, where the mass ratio is 30%. In Figure 14,

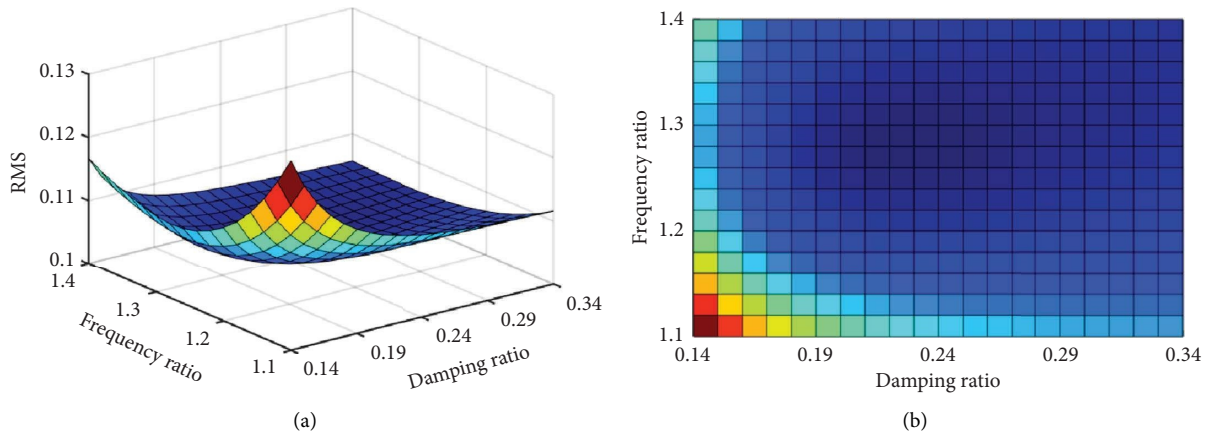

Figure 14: The value of the objective function under different frequency and damping ratio values. (a) 3D view. (b) 2D view.

the frequency and damping ratio that makes the minimum value of the objective function is considered as the optimal design. Based on the optimal design, the effectiveness of ATMD will be evaluated in the following section under the constraints of stroke limitation and control force.

4.3. Vibration Control under Parked and Operational Conditions. The effectiveness of the proposed virtual TMD algorithm in controlling the along-wind vibration of the wind turbine is evaluated in this subsection. The TMD and traditional LQR algorithms [29] are adopted for comparison. In terms of the literature [44], the tuning frequency of TMD is set as the tower fundamental frequency. Also, the TMD mass is selected as percentage of the total mass. Three different mass ratios are selected, 1%, 2%, and 5%, as in similar studies [10, 13]. The vibration control effect of wind turbines will be assessed under parked conditions and operational conditions: $\overline{v}_{\text{Hub}} = 16\,m/s$ at parked maintenance condition (PLC1); $\overline{v}_{\text{Hub}} = 30\,m/s$ at normal parked condition (PLC2); $\overline{v}_{\text{Hub}} = 8\,m/s$ at operational condition (NLC1); and $\overline{v}_{\text{Hub}} = 16\,m/s$ at operational condition (NLC2). The turbulence intensities for these conditions are 0.18. 10 wind field samples are generated by TurbSim [41] for each condition, and the tower top accelerations of the wind turbine are calculated by equations (36) and (41).

4.3.1. Parked Conditions

(1) PLC1. Under this condition, Figure 15 illustrates the tower top accelerations under different control conditions in wind field sample 1. It can be seen from Figure 15(a) that TMD, LQR, and virtual TMD have good vibration control effects. Among them, TMD, LQR, and virtual TMD can reduce the RMS response by 40.56%, 62.77%, and 54.54%, and the maximum response by 29.22%, 55.71%, and 35.92%, respectively. From Figure 15(b), it is seen that the LQR and virtual TMD outperform TMD in mitigating the response at the tower fundamental frequency. The peak value of the TMD controlled wind turbine at the tower fundamental frequency is about 1/9 of the uncontrolled wind turbine, while the peak value of the LQR and virtual TMD is approximately 1/4 of the TMD. Figure 16 shows the stroke and control force of the dampers. It is seen that the stroke of LQR and virtual TMD is within 0.4 m, and the maximum control force is 13 kN.

(2) PLC2. Under this condition, Figure 17 illustrates the tower-top accelerations under different control conditions in wind field sample 1. It can be seen from Figure 17(a) that TMD, LQR, and virtual TMD have good vibration control effects. Among them, TMD, LQR, and virtual TMD can reduce the RMS response by 28.96%, 56.66%, and 44.97%, and the maximum response by 19.46%, 49.76%, and 39.75%, respectively. From Figure 17(b), it is seen that LQR and virtual TMD outperform TMD in mitigating the response at the tower fundamental frequency. The peak value of the TMD controlled wind turbine at the tower fundamental frequency is about 1/8 of the uncontrolled wind turbine, while the peak value of the LQR and virtual TMD is approximately 1/3 of the TMD. Figure 18 shows the stroke and control force of the dampers. It is seen that the stroke of LQR and virtual TMD is within 2.0 m, and the maximum control force is 60 kN.

Figure 19 is the mean square response of the wind turbine acceleration in 10 wind field samples under PLC1 and PLC2 conditions. It is demonstrated that the LQR has a better effect than the virtual TMD in mitigating wind-induced vibration at parked conditions. However, the LQR algorithm, as the optimal feedback control, needs to obtain the full states of the wind turbine. On the contrary, only the acceleration information on the top of the tower or the relative displacement of the active TMD is required for the virtual TMD algorithm. This not only makes the proposed virtual TMD algorithm easier to implement but also reduces the cost of installing sensors.

4.3.2. Operational Conditions

(1) NLC1. Under this condition, Figure 20 illustrates the tower-top accelerations under different control conditions in wind field sample 1. It can be seen from Figure 20(a) that

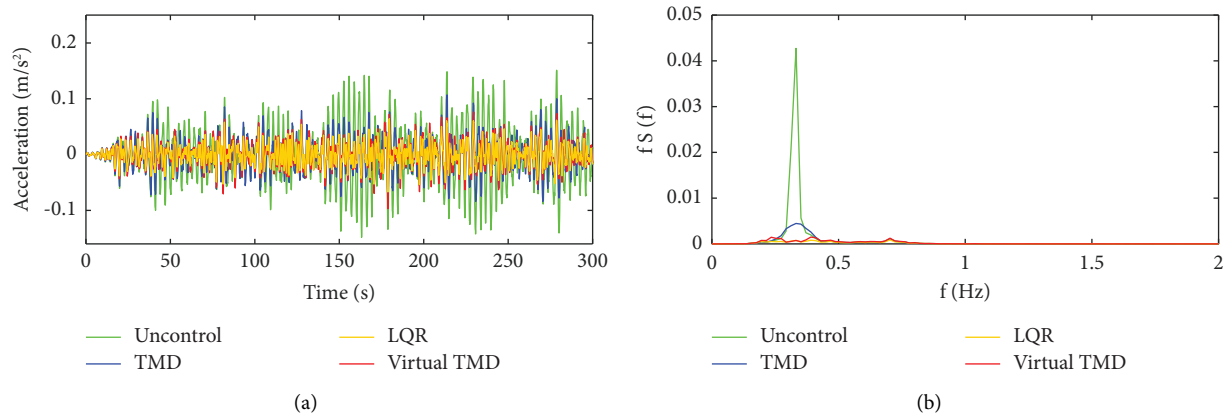

FIGURE 15: Tower-top responses under different control conditions for 2% mass ratio (PLC1, wind field sample 1). (a) Time histories of acceleration. (b) Power spectra of acceleration.

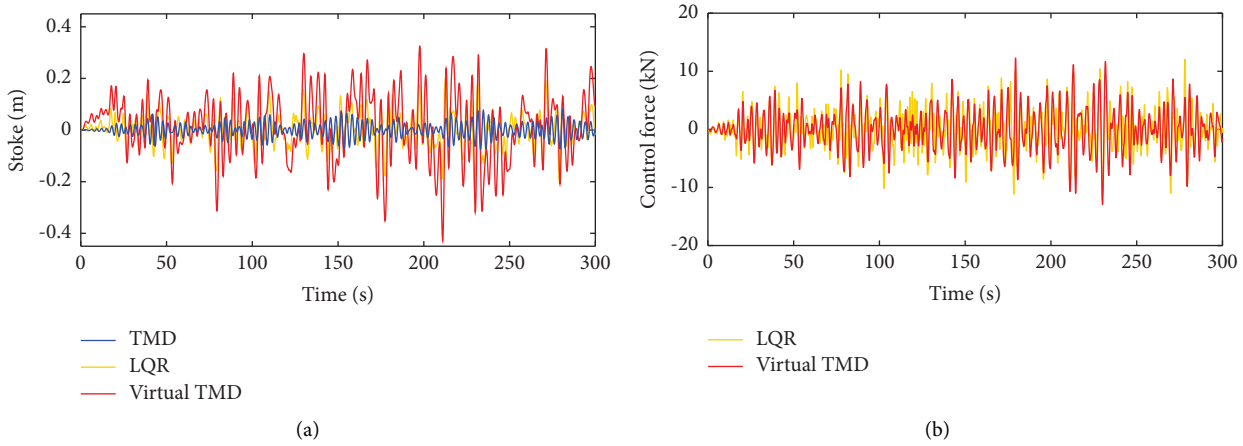

FIGURE 16: Stroke and control force comparison between TMD, LQR, and virtual TMD for 2% mass ratio (PLC1, wind field sample 1). (a) Time histories of stroke. (b) Time histories of control force.

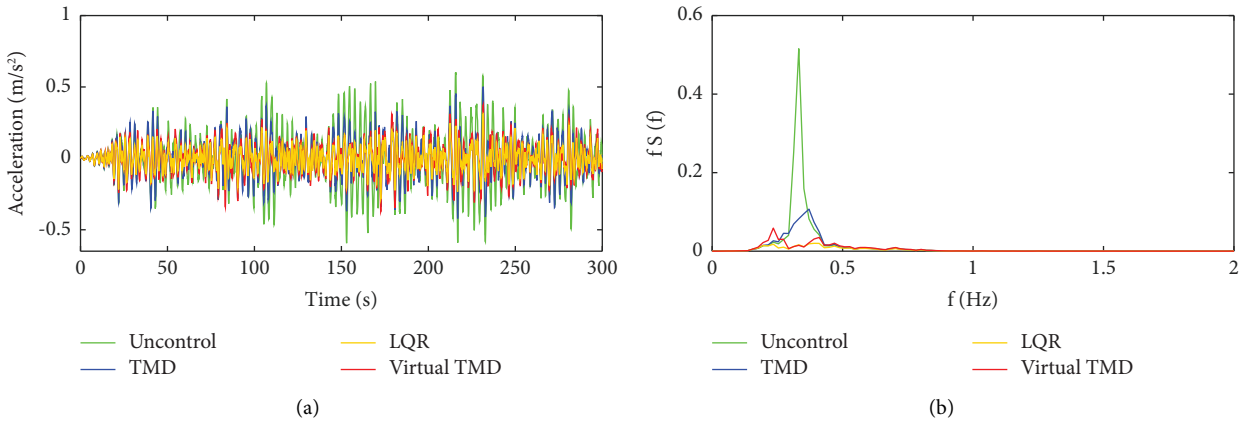

FIGURE 17: Tower-top responses under different control conditions for 2% mass ratio (PLC2, wind field sample 1). (a) Time histories of acceleration. (b) Power spectra of acceleration.

the LQR and virtual TMD still have a good vibration reduction control effect, while TMD has less control effect. Among them, TMD, LQR, and virtual TMD can reduce the RMS response by 5.96%, 33.39%, and 45.11%, and the maximum response by 7.14%, 46.20%, and 54.17%, respectively. It is found that the virtual TMD outperforms LQR in mitigating the tower-top acceleration. The RMS response reduction can be improved by 11.72% using the

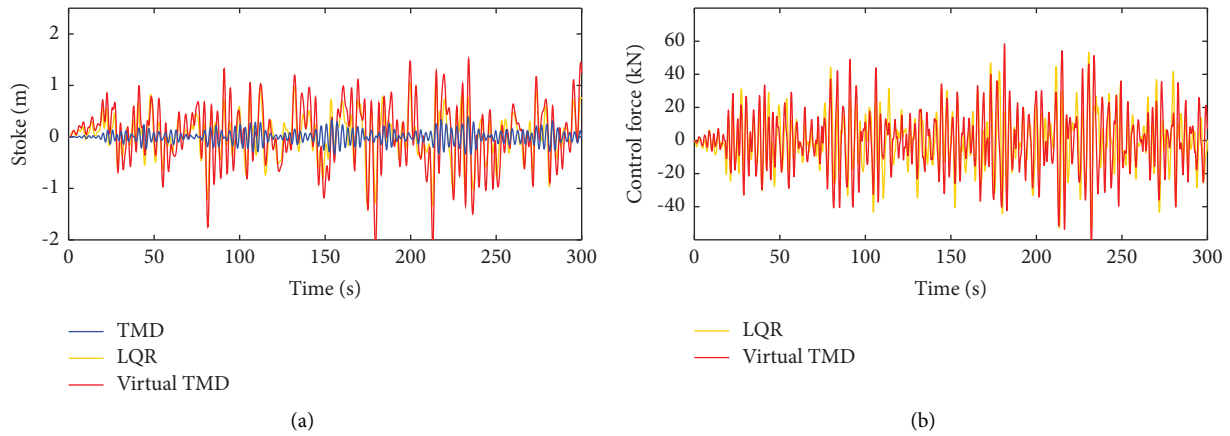

Figure 18: Stroke and control force comparison between TMD, LQR, and virtual TMD for 2% mass ratio (PLC2, wind field sample 1). (a) Time histories of stroke. (b) Time histories of control force.

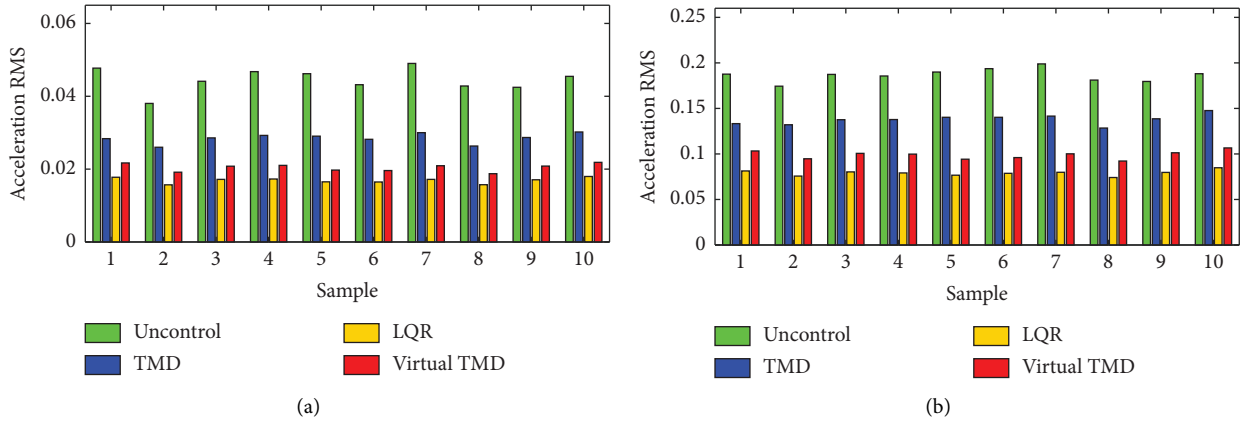

Figure 19: RMS response of tower-top acceleration under 10 wind field samples. (a) PLC1. (b) PLC2.

virtual TMD. From Figure 20(b), it is seen that TMD cannot reduce the tower fundamental frequency and 3P frequency components. The reason is that the tower-top acceleration response at operational condition is dominated by the 3P frequency. In this case, the tower fundamental frequency is not the optimal tuning frequency of TMD. However, LQR and virtual TMD have a good control effect and can significantly reduce the tower fundamental frequency and 3P frequency components. Figure 21 shows the stroke and control force of the dampers. It can be seen that the virtual TMD requires a smaller stroke and control force than the LQR. Also, the stroke of the virtual TMD is within 0.5 m, and the maximum control force is 30 kN.

(2) NLC2. Under this condition, Figure 22 illustrates the tower top accelerations under different control conditions in wind field sample 1. It can be seen from Figure 22(a) that the virtual TMD still has a good vibration reduction control effect, while LQR has less control effect and TMD basically has no control effect. Among them, TMD, LQR, and virtual TMD can reduce the RMS response by 2.41%, 14.16%, and 32.39%, and the maximum response by 2.38%, 15.06%, and 27.53%, respectively. It is found that the virtual TMD outperforms LQR in mitigating the tower-top acceleration. The RMS response reduction can be improved by 18.03% using the virtual TMD algorithm. From Figure 22(b), it is seen that TMD cannot reduce the tower fundamental frequency and 3P frequency components. LQR can significantly reduce the tower fundamental frequency component and cannot reduce the 3P frequency component. Under the NLC2 condition, the 3P frequency is constant at 0.61 Hz, which is not within the effective frequency band of the LQR algorithm. However, the virtual TMD algorithm has a wider band and can significantly reduce the tower fundamental frequency and 3P frequency components. Figure 23 shows the stroke and control force of the dampers. It can be seen that the virtual TMD requires smaller stroke and control force than the LQR. Also, the stroke of the virtual TMD is within 2.0 m, and the maximum control force is 60 kN.

Figure 24 shows the mean square responses of the wind turbine acceleration in 10 wind field samples under NLC1 and NLC2 conditions. It is demonstrated that the virtual TMD has a better effect than the LQR in mitigating wind-induced vibration at operational conditions.

According to the results of 10 wind filed samples under the four conditions, the mean square and maximum control

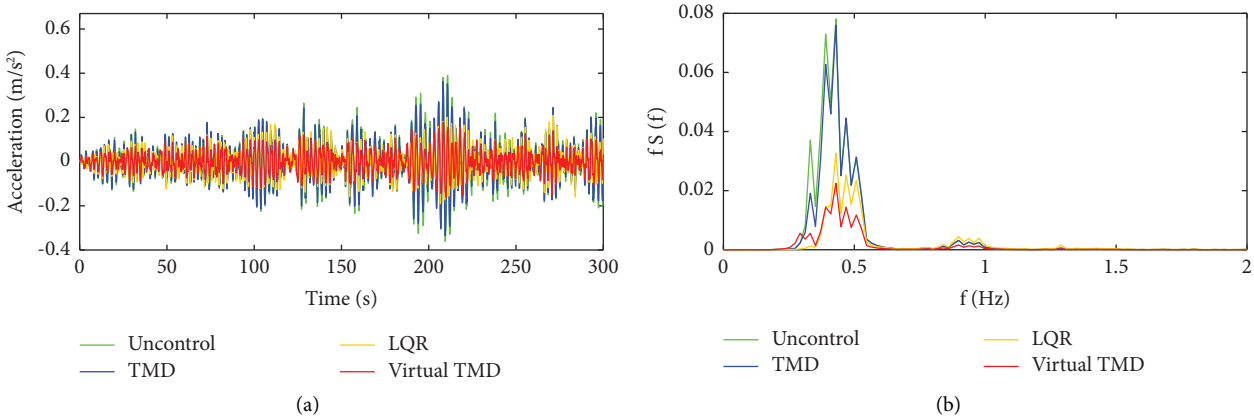

Figure 20: Tower-top responses under different control conditions for 2% mass ratio (NLC1, wind field sample 1). (a) Time histories of acceleration. (b) Power spectra of acceleration.

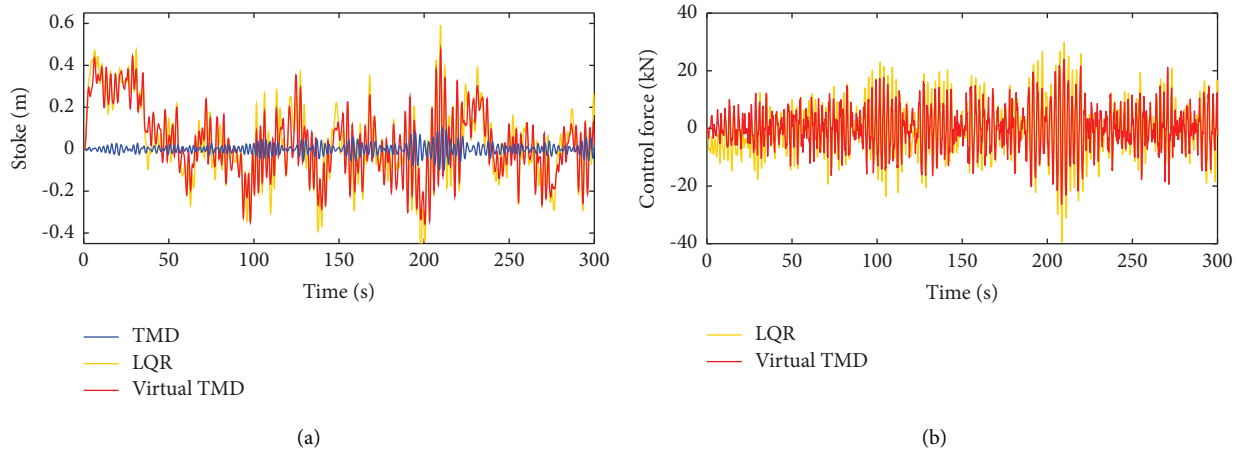

Figure 21: Stroke and control force comparison between TMD, LQR, and virtual TMD for 2% mass ratio (NLC1, wind field sample 1). (a) Time histories of stroke. (b) Time histories of control force.

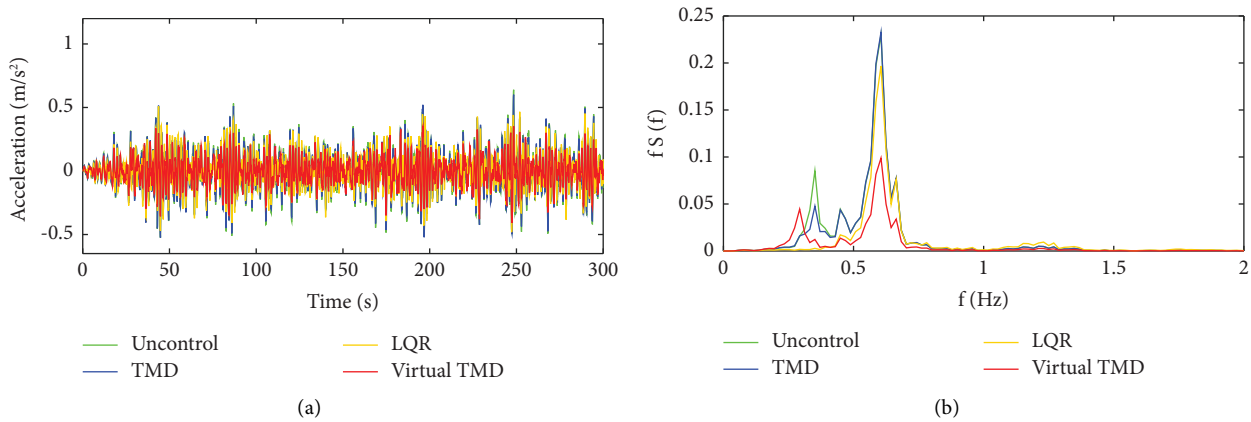

Figure 22: Tower-top responses under different control conditions for 2% mass ratio (NLC2, wind field sample 1). (a) Time histories of acceleration. (b) Power spectra of acceleration.

effects of the accelerations for TMD, LQR, and virtual TMD are obtained, as shown in Table 4. It is seen that the proposed virtual TMD algorithm has a significant control effect both at parked and operational conditions. However, the LQR algorithm and TMD have a less control effect at operational conditions. In order to further verify the control effect of the proposed virtual TMD algorithm, 10 wind field samples with wind speed of 5-30 m/s are generated by TurbSim [41]. The

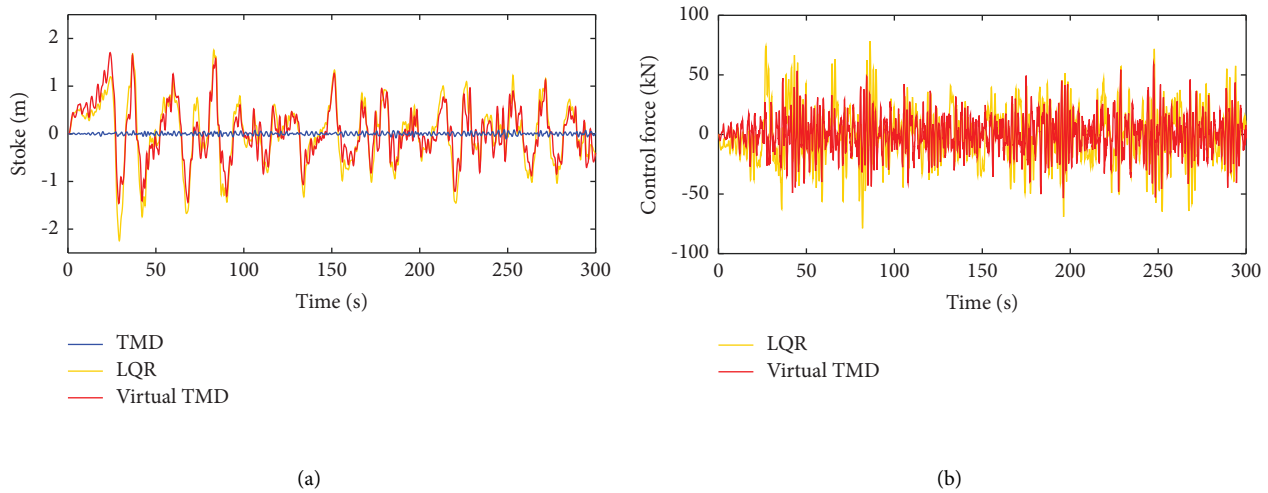

Figure 23: Stroke and control force comparison between TMD, LQR, and virtual TMD for 2% mass ratio (NLC2, wind field sample 1). (a) Time histories of stroke. (b) Time histories of control force.

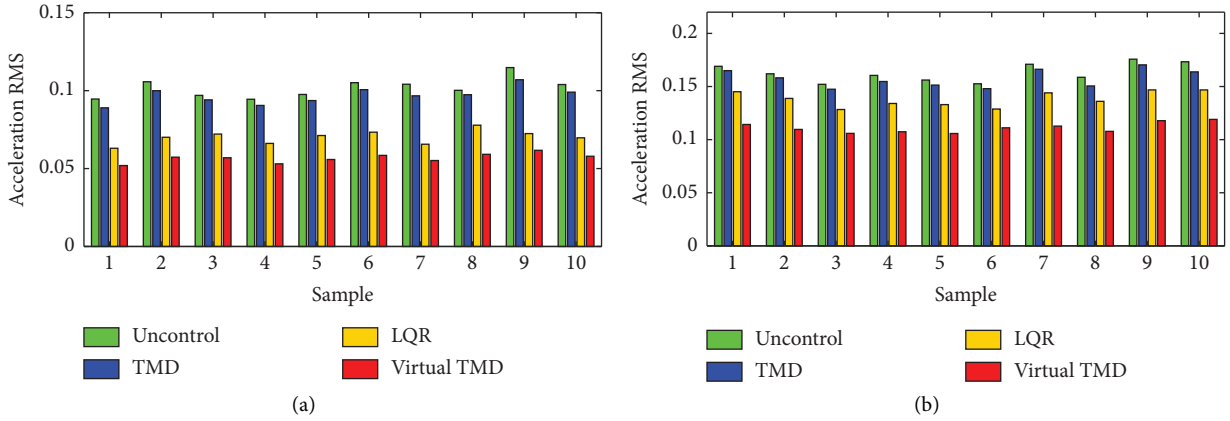

Figure 24: RMS response of tower-top acceleration under 10 wind field samples. (a) NLC1. (b) NLC2.

Table 4: Responses reduction comparison between TMD, LQR, and virtual TMD at park and operational conditions.

	TMD (1%)	TMD (2%)	TMD (5%)	LQR (2%)	Virtual TMD (2%)
RMS response reduction (%)					
PLC1	25.72~34.05	31.64~40.56	40.26~47.92	58.75~64.94	49.64~57.30
PLC2	15.21~23.21	21.51~29.09	31.87~39.38	54.90~59.85	43.33~50.43
NLC1	1.62~4.11	2.80~7.15	5.17~13.33	25.61~36.90	40.98~47.03
NLC2	1.35~4.41	2.34~5.50	4.06~8.37	14.16~16.47	30.37~34.05
Peak response reduction (%)					
PLC1	8.17~34.55	15.87~39.83	23.64~53.40	40.60~61.14	30.89~58.77
PLC2	4.96~28.95	8.67~34.81	20.43~46.19	41.27~61.94	29.21~56.24
NLC1	0.62~5.89	0.97~10.83	2.37~19.64	22.16~46.20	38.23~54.17
NLC2	0.47~3.09	0.79~4.94	1.07~6.86	13.90~29.24	28.13~38.15

turbulence intensities of these wind field samples are 0.18. Then, the tower-top accelerations of the uncontrolled, LQR, and virtual TMD wind turbine are calculated. Figure 25 illustrates the mean square values of tower top acceleration under different control conditions at different wind speeds. From Figure 25, it is seen that the virtual TMD can significantly suppress wind-induced vibrations at different wind speeds, whose control effect can reach more than 30%. It is illustrated that the control effect of LQR is far less than the virtual TMD at operational conditions, especially near the rated wind speed. Figures 26(a)–26(c) illustrate the maximum stroke, control forces, and output power under different control conditions at different wind speeds, respectively. It can be observed that the stroke of the virtual TMD is within 2 m, the control force demand is within 85 kN, and the output power demand is within 80 kW at

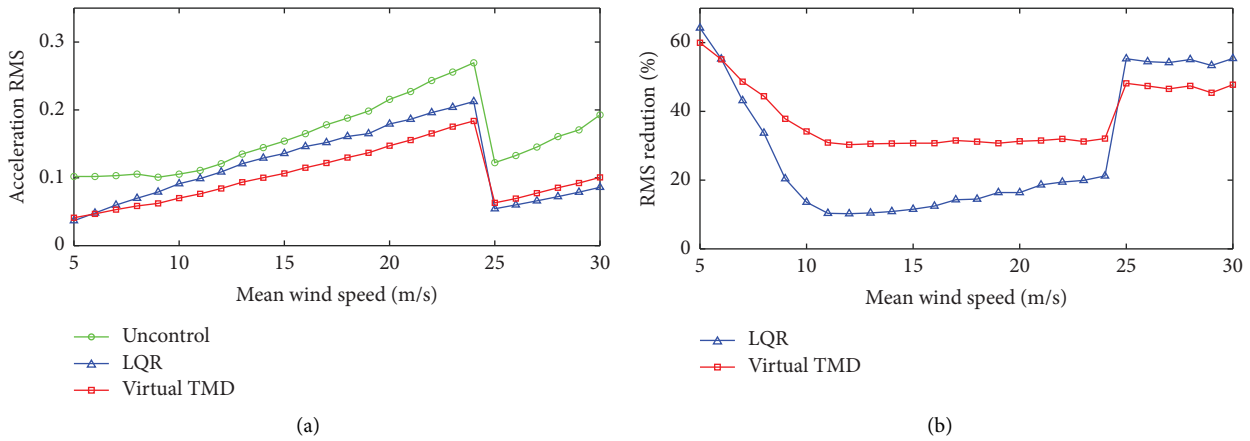

FIGURE 25: RMS response of tower-top acceleration under different wind speeds. (a) RMS response of tower-top acceleration. (b) RMS reduction.

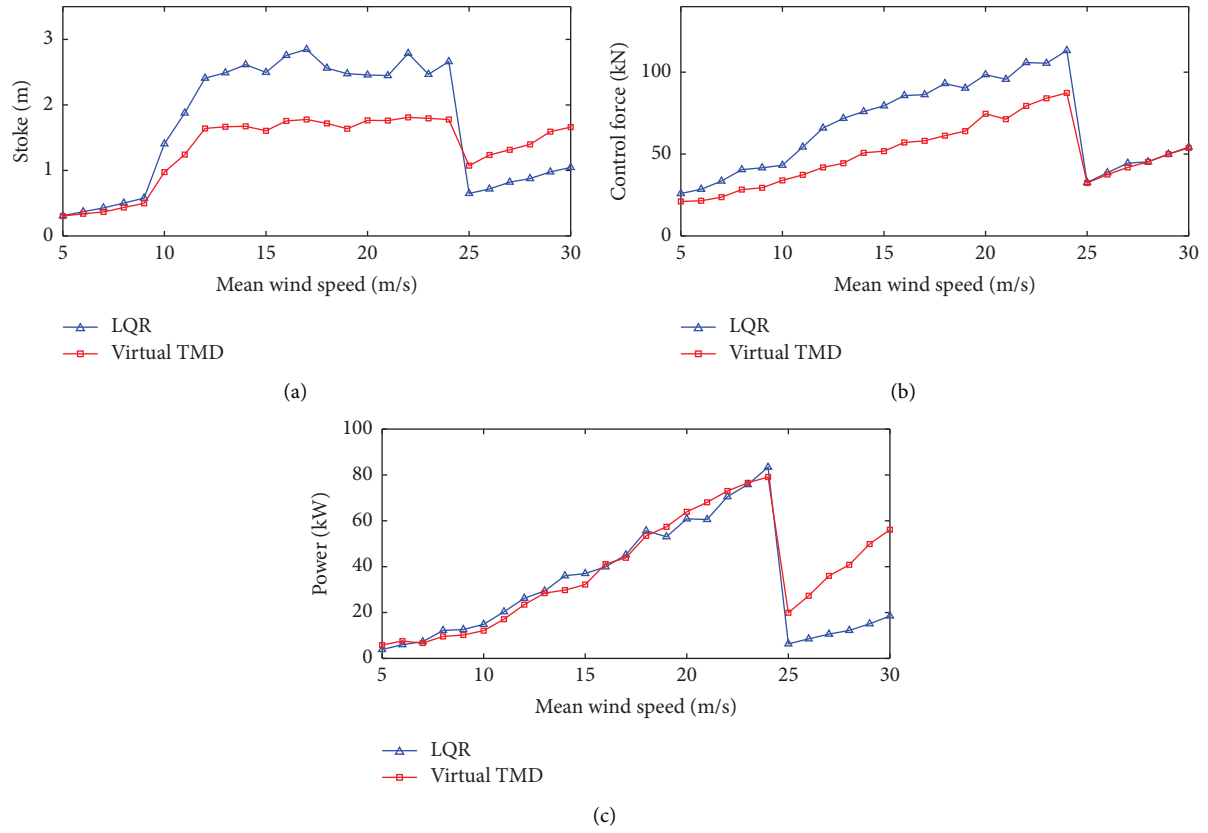

FIGURE 26: LQR and virtual TMD stroke displacement, control force, and output power under different wind speeds. (a) Maximum stroke displacement. (b) Maximum control force. (c) Maximum output power.

Table 5: A comprehensive description of all relevant symbols.

Variable	Description
q_{edi}	Edgewise tip displacement of the ith blade for natural mode 1
q_{fpi}	Flapwise tip displacement of the ith blade for natural mode 1
q_{fpi}	Tower-top base plate displacement in the fore-aft direction for natural mode 1
q_{fpi}	Tower-top base plate displacement in the side-side direction for natural mode 1
θ_{fa}	Longitudinal tower-top rotation
θ_{ss}	Latitudinal tower-top rotation
θ_s	Tilted angle of shaft
x_{hub}	Distance between the hub center and z-axis
z_{hub}	Vertical distance between the hub center and the tower-top base plate
T	Center of the tower top
H	Hub center of mass
B	Center of blade element in undeflected blade

different wind speeds. And the stroke of the LQR is within 3 m, the control force demand is within 115 kN, and the output power demand is within 80 kW at different wind speeds.

5. Conclusions

Based on the holistic coupled dynamic analysis model of wind turbines, this paper proposes a virtual TMD algorithm for ATMD control to reduce the along-wind vibration of the tower. Also, the optimum design of the virtual TMD algorithm has been obtained via a numerical search approach. The performance of this algorithm is compared with passive TMD and the traditional LQR algorithm. According to the results, the following conclusions can be drawn:

(1) Wind turbines exhibit significant time-varying behavior. The along-wind acceleration response of the wind turbine tower is dominated by the natural frequency at parked conditions. However, under operational conditions, the along-wind acceleration response is dominated by the 3P frequency, and the 3P frequency varies with the wind speed.

(2) TMD tuned to the fundamental frequency of the tower has a good control effect at parked conditions, while has a little poor control effect at operational conditions. This suggests that the traditional design approach based on the fundamental frequency of the tower may not be suitable for the wind turbines due to their time-varying characteristics.

(3) The proposed virtual TMD algorithm for ATMD demonstrates excellent adaptability and can significantly reduce vibration in various operating conditions of wind turbines. With the constraints of 80 kW output power and a 2 m stroke limitation, the proposed virtual TMD algorithm has a control effect of more than 30% under various wind speeds.

(4) In comparison with the traditional LQR algorithm, the proposed virtual TMD algorithm has a wider effective bandwidth and only requires the tower-top acceleration information or the relative displacement of the active TMD. The proposed virtual TMD algorithm can improve the reduction effect of the wind turbine response at operational conditions. In addition, the virtual TMD algorithm experiences smaller stroke and control force than the traditional LQR algorithm, which is beneficial to the practical application.

In general, the virtual TMD algorithm outperforms passive TMD and the traditional LQR algorithm in mitigating the vibration of the wind turbine, which has better robustness and can adapt to various conditions. However, it is also worth noting that this paper only focuses on the along-wind vibration control of the wind turbine tower. In addition, references [14, 45] have demonstrated that the performance of the control system can be influenced by soil-structure interaction and wind load uncertainty. Based on this study, future research will be conducted to investigate the bidirectional vibration control of wind turbines, considering soil-structure interaction and the uncertainty of wind loads.

Appendix

Description of Relevant Symbols

A comprehensive description of all relevant symbols is provided in Table 5.

B. Uncontrolled System Matrices

Mass, stiffness, and damping matrix of uncontrolled system:

$$\mathbf{M} = \begin{bmatrix} m_{b,e} & 0 & 0 & 0 & 0 & 0 & -m_{1,7} & -m_{1,8} \\ 0 & m_{b,e} & 0 & 0 & 0 & 0 & -m_{2,7} & -m_{2,8} \\ 0 & 0 & m_{b,e} & 0 & 0 & 0 & -m_{3,7} & -m_{3,8} \\ 0 & 0 & 0 & m_{b,f} & 0 & 0 & m_{4,7} & -m_{4,8} \\ 0 & 0 & 0 & 0 & m_{b,f} & 0 & m_{5,7} & -m_{5,8} \\ 0 & 0 & 0 & 0 & 0 & m_{b,f} & m_{6,7} & -m_{6,8} \\ -m_{1,7} & -m_{2,7} & -m_{3,7} & m_{4,7} & m_{5,7} & m_{6,7} & m_{fa} & 0 \\ -m_{1,8} & -m_{2,8} & -m_{3,8} & -m_{4,8} & -m_{5,8} & -m_{6,8} & 0 & m_{ss} \end{bmatrix}, \tag{B.1}$$

where

$$m_{b,e}=\int_0^R \overline{m}(r)\phi_{1e}^2\mathrm{d}r, m_{b,f}=\int_0^R \overline{m}(r)\phi_{1f}^2\mathrm{d}r, m_{bj2,r}=\int_0^R \overline{m}(r)\left(r+R_{\mathrm{hub}}\right)^2\mathrm{d}r,$$

$$m_{j,7}=\int_0^R \overline{m}(r)\phi_{1e}\left(\left.\frac{\mathrm{d}\phi_{fa}}{\mathrm{d}z}\right|_{z=h}\left(x_{\mathrm{hub}}\sin\varphi_j\cos\theta_s+z_{\mathrm{hub}}\sin\varphi_j\sin\theta_s\right)+\sin\varphi_j\sin\theta_s\right)\mathrm{d}r,$$

$$m_{j+3,7}=\int_0^R \overline{m}(r)\phi_{1f}\left(\left.\frac{\mathrm{d}\phi_{fa}}{\mathrm{d}z}\right|_{z=h}\left((r+R_{\mathrm{hub}})\cos\varphi_j+z_{\mathrm{hub}}\cos\theta_s-x_{\mathrm{hub}}\sin\theta_s\right)+\cos\theta_s\right)\mathrm{d}r,$$

$$m_{j,8}=\int_0^R \overline{m}(r)\phi_{1e}\left(\left.\frac{\mathrm{d}\phi_{ss}}{\mathrm{d}z}\right|_{z=h}\left((r+R_{\mathrm{hub}})\cos\theta_s+z_{\mathrm{hub}}\cos\varphi_j\right)+\cos\varphi_j\right)\mathrm{d}r, m_{j+3,8}=\int_0^R \overline{m}(r)\phi_{1f}\left(\left.\frac{\mathrm{d}\phi_{ss}}{\mathrm{d}z}\right|_{z=h}(r+R_{\mathrm{hub}})\sin\varphi_j\sin\theta_s\right)\mathrm{d}r,$$

$$m_{j+3,k7}=\int_0^R \overline{m}(r)\phi_{1f}\left(\left.\frac{\mathrm{d}\phi_{fa}}{\mathrm{d}z}\right|_{z=h}(r+R_{\mathrm{hub}})\cos\varphi_j\right)\mathrm{d}r, m_{j,k8}=\int_0^R \overline{m}(r)\phi_{1e}\left(1+\left.\frac{\mathrm{d}\phi_{ss}}{\mathrm{d}z}\right|_{z=h}z_{\mathrm{hub}}\right)\cos\varphi_j\mathrm{d}r,$$

$$M_{2,fa}=\int_0^h \overline{M}(z)\phi_{fa}^2\mathrm{d}z, M_{2,ss}=\int_0^h \overline{M}(z)\phi_{ss}^2\mathrm{d}z, M_{2,fa}=\int_0^h \overline{M}(z)\phi_{fa}^2\mathrm{d}z, M_{2,ss}=\int_0^h \overline{M}(z)\phi_{ss}^2\mathrm{d}z,$$

$$m_{bj2,fa}=\int_0^R \overline{m}(r)\left(\left.\frac{\mathrm{d}\phi_{fa}}{\mathrm{d}z}\right|_{z=h}(r+R_{\mathrm{hub}})\right)^2\mathrm{d}r, m_{bj2,ss}=\int_0^R \overline{m}(r)\left(\left.\frac{\mathrm{d}\phi_{ss}}{\mathrm{d}z}\right|_{z=h}(r+R_{\mathrm{hub}})\right)^2\mathrm{d}r,$$

$$m_{fa}=3m_b\left(1+\left.\frac{\mathrm{d}\phi_{fa}}{\mathrm{d}z}\right|_{z=h}z_{\mathrm{hub}}\right)^2+3m_b\left(\left.\frac{\mathrm{d}\phi_{fa}}{\mathrm{d}z}\right|_{z=h}x_{\mathrm{hub}}\right)^2+\frac{3}{2}m_{bj2,fa}+M_{2,fa}$$
$$+M_n\left(\left(\left.\frac{\mathrm{d}\phi_{fa}}{\mathrm{d}z}\right|_{z=h}x_{\mathrm{nac}}\right)^2+\left(1+\left.\frac{\mathrm{d}\phi_{fa}}{\mathrm{d}z}\right|_{z=h}z_{\mathrm{nac}}\right)^2\right)+M_h\left(\left(\left.\frac{\mathrm{d}\phi_{fa}}{\mathrm{d}z}\right|_{z=h}x_{\mathrm{hub}}\right)^2+\left(1+\left.\frac{\mathrm{d}\phi_{fa}}{\mathrm{d}z}\right|_{z=h}z_{\mathrm{hub}}\right)^2\right),$$

$$m_{ss}=3m_b\left(1+\left.\frac{\mathrm{d}\phi_{ss}}{\mathrm{d}z}\right|_{z=h}z_{\mathrm{hub}}\right)^2+\frac{3}{2}m_{bj2,ss}\left(1+\cos^2\theta_s\right)+M_n\left(1+\left.\frac{\mathrm{d}\phi_{ss}}{\mathrm{d}z}\right|_{z=h}z_{\mathrm{nac}}\right)^2+M_h\left(1+\left.\frac{\mathrm{d}\phi_{ss}}{\mathrm{d}z}\right|_{z=h}z_{\mathrm{hub}}\right)^2+M_{2,ss},$$

$$\mathbf{K}=\begin{bmatrix}
K_{b1,eg} & 0 & 0 & 0 & 0 & 0 & \Omega^2m_{1,7} & \Omega^2m_{1,k8}\\
0 & K_{b2,eg} & 0 & 0 & 0 & 0 & \Omega^2m_{2,7} & \Omega^2m_{2,k8}\\
0 & 0 & K_{b3,eg} & 0 & 0 & 0 & \Omega^2m_{3,7} & \Omega^2m_{3,k8}\\
0 & 0 & 0 & K_{b1,fp} & 0 & 0 & -\Omega^2m_{4,k7} & \Omega^2m_{4,8}\\
0 & 0 & 0 & 0 & K_{b2,fp} & 0 & -\Omega^2m_{5,k7} & \Omega^2m_{5,8}\\
0 & 0 & 0 & 0 & 0 & K_{b3,fp} & -\Omega^2m_{6,k7} & \Omega^2m_{6,8}\\
0 & 0 & 0 & 0 & 0 & 0 & K_{fa} & 0\\
0 & 0 & 0 & 0 & 0 & 0 & 0 & K_{ss}
\end{bmatrix}, \tag{B.2}$$

where

$$k_{bj,eg} = k_{eg} + k_{ge,eg} - k_{gr,eg}\cos\varphi_j - \Omega^2 m_{b,e}, k_{\text{bjfp}} = k_{fp} + k_{\text{gefp}} - k_{\text{grfp}}\cos\varphi_j,$$

$$k_7 = \int_0^h EI_t\left(\frac{\mathrm{d}^2\phi_{fa}}{\mathrm{d}z^2}\right)^2\mathrm{d}z, k_8 = \int_0^h EI_t\left(\frac{\mathrm{d}^2\phi_{ss}}{\mathrm{d}z^2}\right)^2\mathrm{d}z,$$

$$k_{\text{gravity1}} = g\left[M_n\int_0^h\left(\frac{\mathrm{d}\phi_{fa}}{\mathrm{d}z}\right)^2\mathrm{d}z + \int_0^h\overline{M}\int_0^z\left(\frac{\mathrm{d}\phi_{fa}}{\mathrm{d}z}\right)^2\mathrm{d}z'\mathrm{d}z\right], k_{\text{gravity2}} = g\left[M_n\int_0^h\left(\frac{\mathrm{d}\phi_{ss}}{\mathrm{d}z}\right)^2\mathrm{d}z + \int_0^h\overline{M}\int_0^z\left(\frac{\mathrm{d}\phi_{ss}}{\mathrm{d}z}\right)^2\mathrm{d}z'\mathrm{d}z\right],$$

$$k_{fa} = k_7 - k_{\text{gravity1}} - \frac{3}{2}\Omega^2 m_{bj2,fa}$$

$$- 3\Omega^2 m_b\left(\sin^2\theta_s + \left(\left.\frac{\mathrm{d}\phi_{fa}}{\mathrm{d}z}\right|_{z=h} x_{\text{hub}}\cos\theta_s + \left.\frac{\mathrm{d}\phi_{fa}}{\mathrm{d}z}\right|_{z=h} z_{\text{hub}}\sin\theta_s\right)^2 + 2\left.\frac{\mathrm{d}\phi_{fa}}{\mathrm{d}z}\right|_{z=h}\cos\theta_s\sin\theta_s\left(x_{\text{hub}} + z_{\text{hub}}\right)\right),$$

$$k_{ss} = k_8 - k_{\text{gravity2}} - 3\Omega^2 m_b\left(1 + \left.\frac{\mathrm{d}\phi_{ss}}{\mathrm{d}z}\right|_{z=h} Z_{\text{hub}}\right)^2 - \frac{3}{2}\Omega^2 m_{bj2,fa}\sin^2\theta_s,$$

$$\mathbf{C} = \begin{bmatrix} c_{b,eg} & 0 & 0 & 0 & 0 & 0 & -2\Omega m_{1,c7} & 2\Omega m_{1,c8} \\ 0 & c_{b,eg} & 0 & 0 & 0 & 0 & -2\Omega m_{2,c7} & 2\Omega m_{2,c8} \\ 0 & 0 & c_{b,eg} & 0 & 0 & 0 & -2\Omega m_{3,c7} & 2\Omega m_{3,c8} \\ 0 & 0 & 0 & c_{b,fp} & 0 & 0 & -2\Omega m_{4,c7} & -2\Omega m_{4,c8} \\ 0 & 0 & 0 & 0 & c_{b,fp} & 0 & -2\Omega m_{5,c7} & -2\Omega m_{5,c8} \\ 0 & 0 & 0 & 0 & 0 & c_{b,fp} & -2\Omega m_{6,c7} & -2\Omega m_{6,c8} \\ 0 & 0 & 0 & 0 & 0 & 0 & c_{fa} & c_{7,8} \\ 0 & 0 & 0 & 0 & 0 & 0 & c_{7,8} & c_{ss} \end{bmatrix}, \tag{B.3}$$

where

$$m_{j,c7} = \int_0^R \overline{m}(r)\phi_{1e}\left(\left.\frac{\mathrm{d}\phi_{fa}}{\mathrm{d}z}\right|_{z=h}\left(x_{\text{hub}}\cos\varphi_j\cos\theta_s + z_{\text{hub}}\cos\varphi_j\sin\theta_s\right) + \cos\varphi_j\sin\theta_s\right)\mathrm{d}r,$$

$$m_{j+3,c7} = \int_0^R \overline{m}(r)\phi_{1f}\left(\left.\frac{\mathrm{d}\phi_{fa}}{\mathrm{d}z}\right|_{z=h}(r + R_{\text{hub}})\sin\varphi_j\right)\mathrm{d}r,$$

$$m_{j,c8} = \int_0^R \overline{m}(r)\phi_{1e}\left(1 + \left.\frac{\mathrm{d}\phi_{ss}}{\mathrm{d}z}\right|_{z=h} z_{\text{hub}}\right)\sin\varphi_j\mathrm{d}r, \tag{B.4}$$

$$m_{j+3,c8} = \int_0^R \overline{m}(r)\phi_{1f}\left(\left.\frac{\mathrm{d}\phi_{ss}}{\mathrm{d}z}\right|_{z=h}(r + R_{\text{hub}})\cos\varphi_j\sin\theta_s\right)\mathrm{d}r,$$

$$c_{7,8} = -3\Omega\left.\frac{\mathrm{d}\phi_{fa}}{\mathrm{d}z}\right|_{z=h}\left.\frac{\mathrm{d}\phi_{ss}}{\mathrm{d}z}\right|_{z=h} m_{bj2,r} - 6\Omega m_b\left(1 + \left(\frac{\mathrm{d}\phi_{ss}}{\mathrm{d}z}\right)_{z=h} z_{\text{hub}}\right)\left(\left.\frac{\mathrm{d}\phi_{ss}}{\mathrm{d}z}\right|_{z=h}\left(x_{\text{hub}}\cos\theta_s + z_{\text{hub}}\sin\theta_s\right) + \sin\theta_s\right).$$

C. ATMD Controlled System Matrices

Mass, stiffness, and damping matrix of ATMD controlled system:

$$\mathbf{M}_1 = \begin{bmatrix} m_{b,e} & 0 & 0 & 0 & 0 & 0 & -m_{1,7} & -m_{1,8} & 0 \\ 0 & m_{b,e} & 0 & 0 & 0 & 0 & -m_{2,7} & -m_{2,8} & 0 \\ 0 & 0 & m_{b,e} & 0 & 0 & 0 & -m_{3,7} & -m_{3,8} & 0 \\ 0 & 0 & 0 & m_{b,f} & 0 & 0 & m_{4,7} & -m_{4,8} & 0 \\ 0 & 0 & 0 & 0 & m_{b,f} & 0 & m_{5,7} & -m_{5,8} & 0 \\ 0 & 0 & 0 & 0 & 0 & m_{b,f} & m_{6,7} & -m_{6,8} & 0 \\ -m_{1,7} & -m_{2,7} & -m_{3,7} & m_{4,7} & m_{5,7} & m_{6,7} & m_{fa} & 0 & 0 \\ -m_{1,8} & -m_{2,8} & -m_{3,8} & -m_{4,8} & -m_{5,8} & -m_{6,8} & 0 & m_{ss} & 0 \\ 0 & 0 & 0 & 0 & 0 & 0 & m_{\text{tmd}} & 0 & m_{\text{tmd}} \end{bmatrix}, \tag{C.1}$$

$$\mathbf{K}_1 = \begin{bmatrix} K_{b1,eg} & 0 & 0 & 0 & 0 & 0 & \Omega^2 m_{1,7} & \Omega^2 m_{1,k8} & 0 \\ 0 & K_{b2,eg} & 0 & 0 & 0 & 0 & \Omega^2 m_{2,7} & \Omega^2 m_{2,k8} & 0 \\ 0 & 0 & K_{b3,eg} & 0 & 0 & 0 & \Omega^2 m_{3,7} & \Omega^2 m_{3,k8} & 0 \\ 0 & 0 & 0 & K_{b1,fp} & 0 & 0 & -\Omega^2 m_{4,k7} & \Omega^2 m_{4,8} & 0 \\ 0 & 0 & 0 & 0 & K_{b2,fp} & 0 & -\Omega^2 m_{5,k7} & \Omega^2 m_{5,8} & 0 \\ 0 & 0 & 0 & 0 & 0 & K_{b3,fp} & -\Omega^2 m_{6,k7} & \Omega^2 m_{6,8} & 0 \\ 0 & 0 & 0 & 0 & 0 & 0 & K_{fa} & 0 & -k_{\text{TMD}} \\ 0 & 0 & 0 & 0 & 0 & 0 & 0 & K_{ss} & 0 \\ 0 & 0 & 0 & 0 & 0 & 0 & 0 & 0 & k_{\text{TMD}} \end{bmatrix}, \tag{C.2}$$

$$\mathbf{C}_1 = \begin{bmatrix} c_{b,eg} & 0 & 0 & 0 & 0 & 0 & -2\Omega m_{1,c7} & 2\Omega m_{1,c8} & 0 \\ 0 & c_{b,eg} & 0 & 0 & 0 & 0 & -2\Omega m_{2,c7} & 2\Omega m_{2,c8} & 0 \\ 0 & 0 & c_{b,eg} & 0 & 0 & 0 & -2\Omega m_{3,c7} & 2\Omega m_{3,c8} & 0 \\ 0 & 0 & 0 & c_{b,fp} & 0 & 0 & -2\Omega m_{4,c7} & -2\Omega m_{4,c8} & 0 \\ 0 & 0 & 0 & 0 & c_{b,fp} & 0 & -2\Omega m_{5,c7} & -2\Omega m_{5,c8} & 0 \\ 0 & 0 & 0 & 0 & 0 & c_{b,fp} & -2\Omega m_{6,c7} & -2\Omega m_{6,c8} & 0 \\ 0 & 0 & 0 & 0 & 0 & 0 & c_{fa} & c_{7,8} & -c_{\text{TMD}} \\ 0 & 0 & 0 & 0 & 0 & 0 & c_{7,8} & c_{ss} & 0 \\ 0 & 0 & 0 & 0 & 0 & 0 & 0 & 0 & c_{\text{TMD}} \end{bmatrix}. \tag{C.3}$$

Data Availability

The datasets generated and/or analyzed during the present study are available from the corresponding authors on reasonable request.

Conflicts of Interest

The authors declare that they have no conflicts of interest.

Acknowledgments

The support by the National Natural Science Foundation of China (Grant nos. 52008061 and 52178456), 111 Base Project (B18062), Jinan Innovation Team Project (2020GXRC045), and Science and Technology Innovation Guidance Special Project (cstc2019yszx-jcyjX005) are greatly acknowledged.

References

[1] M. Hutchinson and F. Zhao, *Global Wind Report 2023*, Global Wind Energy Council, Brussels, Belgium, 2023.

[2] R. H. Wiser, *Land-Based Wind Market Report: 2021 Edition*, Lawrence Berkeley National Laboratory(LBNL), Berkeley, CA, USA, 2021.

[3] L. Dueñas-Osorio and B. Basu, "Unavailability of wind turbines due to wind-induced accelerations," *Engineering Structures*, vol. 30, no. 4, pp. 885–893, 2008.

[4] S. Colwell and B. Basu, "Tuned liquid column dampers in offshore wind turbines for structural control," *Engineering Structures*, vol. 31, no. 2, pp. 358–368, 2009.

[5] J. S. Chou and W. T. Tu, "Failure analysis and risk management of a collapsed large wind turbine tower," *Engineering Failure Analysis*, vol. 18, no. 1, pp. 295–313, 2011.

[6] Caithness Wind Farm Information Forum, "Summary of wind turbine accident data to 31," 2023, https://scotlandagainstspin.org/turbine-accident-statistics/.

[7] B. Fitzgerald and B. Basu, "Vibration control of wind turbines: recent advances and emerging trends," *International Journal of Sustainable Materials and Structural Systems*, vol. 4, no. 2/3/4, pp. 347–372, 2020.

[8] H. Zuo, K. Bi, and H. Hao, "A state-of-the-art review on the vibration mitigation of wind turbines," *Renewable and Sustainable Energy Reviews*, vol. 121, Article ID 109710, 2020.

[9] P. J. Murtagh, A. Ghosh, B. Basu, and B. M. Broderick, "Passive control of wind turbine vibrations including blade/tower interaction and rotationally sampled turbulence," *Wind Energy*, vol. 11, no. 4, pp. 305–317, 2008.

[10] M. A. Lackner and M. A. Rotea, "Passive structural control of offshore wind turbines," *Wind Energy*, vol. 14, no. 3, pp. 373–388, 2011.

[11] C. Li, T. Zhuang, S. Zhou, Y. Xiao, and G. Hu, "Passive vibration control of a semi-submersible floating offshore wind turbine," *Applied Sciences*, vol. 7, no. 6, p. 509, 2017.

[12] J. J. Yang and E. M. He, "Coupled modeling and structural vibration control for floating offshore wind turbine," *Renewable Energy*, vol. 157, pp. 678–694, 2020.

[13] M. Ghassempour, G. Failla, and F. Arena, "Vibration mitigation in offshore wind turbines via tuned mass damper," *Engineering Structures*, vol. 183, pp. 610–636, 2019.

[14] S. Gaur, S. Elias, T. Höbbel, V. A. Matsagar, and K. Thiele, "Tuned mass dampers in wind response control of wind turbine with soil-structure interaction," *Soil Dynamics and Earthquake Engineering*, vol. 132, Article ID 106071, 2020.

[15] H. Zuo, K. Bi, and H. Hao, "Using multiple tuned mass dampers to control offshore wind turbine vibrations under multiple hazards," *Engineering Structures*, vol. 141, pp. 303–315, 2017.

[16] S. Sarkar and B. Fitzgerald, "Vibration control of spar-type floating offshore wind turbine towers using a tuned mass-damper-inerter," *Structural Control and Health Monitoring*, vol. 27, no. 1, Article ID e2471, 2020.

[17] Z. Zhang and B. Fitzgerald, "Tuned mass-damper-inerter (TMDI) for suppressing edgewise vibrations of wind turbine blades," *Engineering Structures*, vol. 221, Article ID 110928, 2020.

[18] Z. Zhang and C. Høeg, "Inerter-enhanced tuned mass damper for vibration damping of floating offshore wind turbines," *Ocean Engineering*, vol. 223, Article ID 108663, 2021.

[19] J. Chen and C. T. Georgakis, "Tuned rolling-ball dampers for vibration control in wind turbines," *Journal of Sound and Vibration*, vol. 332, no. 21, pp. 5271–5282, 2013.

[20] C. Sun and V. Jahangiri, "Bi-directional vibration control of offshore wind turbines using a 3D pendulum tuned mass damper," *Mechanical Systems and Signal Processing*, vol. 105, pp. 338–360, 2018.

[21] A. F. Mensah and L. Dueñas-Osorio, "Improved reliability of wind turbine towers with tuned liquid column dampers (TLCDs)," *Structural Safety*, vol. 47, pp. 78–86, 2014.

[22] J. Chen, C. Yuan, J. Li, and Q. Xu, "Semi-active fuzzy control of edgewise vibrations in wind turbine blades under extreme wind," *Journal of Wind Engineering and Industrial Aerodynamics*, vol. 147, pp. 251–261, 2015.

[23] C. Sun, "Semi-active control of monopile offshore wind turbines under multi-hazards," *Mechanical Systems and Signal Processing*, vol. 99, pp. 285–305, 2018.

[24] A. Hemmati and E. Oterkus, "Semi-active structural control of offshore wind turbines considering damage development," *Journal of Marine Science and Engineering*, vol. 6, no. 3, p. 102, 2018.

[25] M. A. Lackner and M. A. Rotea, "Structural control of floating wind turbines," *Mechatronics*, vol. 21, no. 4, pp. 704–719, 2011.

[26] X. Li and H. Gao, "Load mitigation for a floating wind turbine via generalized structural control," *IEEE Transactions on Industrial Electronics*, vol. 63, no. 1, pp. 332–342, 2016.

[27] M. L. Brodersen, A. S. Bjørke, and J. Høgsberg, "Active tuned mass damper for damping of offshore wind turbine vibrations," *Wind Energy*, vol. 20, no. 5, pp. 783–796, 2017.

[28] B. Fitzgerald, B. Basu, and S. R. Nielsen, "Active tuned mass dampers for control of in-plane vibrations of wind turbine blades," *Structural Control and Health Monitoring*, vol. 20, no. 12, pp. 1377–1396, 2013.

[29] B. Fitzgerald, S. Sarkar, and A. Staino, "Improved reliability of wind turbine towers with active tuned mass dampers (ATMDs)," *Journal of Sound and Vibration*, vol. 419, pp. 103–122, 2018.

[30] Y. Hu, M. Z. Chen, and C. Li, "Active structural control for load mitigation of wind turbines via adaptive sliding-mode approach," *Journal of the Franklin Institute*, vol. 354, no. 11, pp. 4311–4330, 2017.

[31] T. Burton, N. Jenkins, D. Sharpe, and E. Bossanyi, *Wind Energy Handbook*, John Wiley and Sons, Hoboken, NJ, USA, 2nd edition, 2011.

[32] K. Gong and X. Chen, "Improved modeling of equivalent static loads on wind turbine towers," *Wind and Structures*, vol. 20, no. 5, pp. 609–622, 2015.

[33] P. J. Murtagh, B. Basu, and B. M. Broderick, "Along-wind response of a wind turbine tower with blade coupling subjected to rotationally sampled wind loading," *Engineering Structures*, vol. 27, no. 8, pp. 1209–1219, 2005.

[34] K. T. Kim and C. W. Lee, "Structural vibration analysis of large-scale wind turbines considering periodically time-varying parameters," *13th World Congress in Mechanism and Machine Science*, vol. 15, pp. 1–9, 2011.

[35] J. Jonkman and L. B. Marshall, "FAST User's Guide," Technical Report, National Renewable Energy Laboratory, Golden, CO, USA, 2005.

[36] Z. Zhang, *Passive and Active Vibration Control of Renewable Energy Structures*, Aalborg Universitetsforlag, Aalborg, Denmark, 2015.

[37] J. M. Jonkman, *Modeling of the UAE Wind Turbine for Refinement of FAST_AD*, National Renewable Energy Lab, Golden, CO, USA, 2003.

[38] J. Jonkman, S. Butterfield, W. Musial, and G. Scott, "Definition of a 5-MW Reference Wind Turbine for Offshore

Systems Development," Technical Report, National Renewable Energy Lab, Golden, CO, USA, 2009.
[39] M. Hansen, *Aerodynamics of Wind Turbines*, Routledge, England, UK, 3rd edition, 2015.
[40] Iec Wind turbines, *Part 3: Design Requirements for Offshore Wind Turbines*, International Electrotechnical Commission, Geneva, Switzerland, 2009.
[41] B. J. Jonkman and L. Kilcher, "TurbSim User's Guide: Version 1.06.00," Technical Report, National Renewable Energy Laboratory, Golden, CO, USA, 2012.
[42] J. D. Holmes, *Wind Loading of Structures*, CRC Press, Boca Raton, FL, USA, 2018.
[43] I. G. Currie, *Fundamental Mechanics of Fluids*, CRC Press, Boca Raton, FL, USA, 4th edition, 2016.
[44] H. C. Tsai, G. C. Lin, and G. C. Lin, "Optimum tuned-mass dampers for minimizing steady-state response of support-excited and damped systems," *Earthquake Engineering and Structural Dynamics*, vol. 22, no. 11, pp. 957–973, 1993.
[45] S. Elias, V. Matsagar, and T. K. Datta, "Along-wind response control of chimneys with distributed multiple tuned mass dampers," *Structural Control and Health Monitoring*, vol. 26, no. 1, Article ID e2275, 2019.